ACCRETION IN THE EARLY KUIPER BELT. I. COAGULATION AND VELOCITY EVOLUTION

SCOTT J. KENYON

Harvard-Smithsonian Center for Astrophysics, 60 Garden Street, Cambridge, MA 02138; skenyon@cfa.harvard.edu

AND

JANE X. LUU

Department of Astronomy, Harvard University, 60 Garden Street, Cambridge, MA 02138; jluu@cfa.harvard.edu

ABSTRACT

We describe planetesimal accretion calculations in the Kuiper Belt. Our evolution code simulates planetesimal growth in a single annulus and includes velocity evolution but not fragmentation. Test results match analytic solutions and duplicate previous simulations at 1 AU. In the Kuiper Belt, simulations without velocity evolution produce a single runaway body with a radius $r_i \gtrsim 1000$ km on a timescale $\tau_r \propto M_0^{-1} e_0^x$, where M_0 is the initial mass in the annulus, e_0 is the initial eccentricity of the planetesimals, and $x \approx 1$–2. Runaway growth occurs in 100 Myr for $M_0 \approx 10 M_E$ and $e_0 \approx 10^{-3}$ in a 6 AU annulus centered at 35 AU. This mass is close to the amount of dusty material expected in a minimum-mass solar nebula extrapolated into the Kuiper Belt. Simulations with velocity evolution produce runaway growth on a wide range of timescales. Dynamical friction and viscous stirring increase particle velocities in models with large (8 km radius) initial bodies. This velocity increase delays runaway growth by a factor of 2 compared with models without velocity evolution. In contrast, collisional damping dominates over dynamical friction and viscous stirring in models with small (80–800 m) initial bodies. Collisional damping decreases the timescale to runaway growth by factors of 4–10 relative to constant-velocity calculations. Simulations with minimum-mass solar nebulae, $M_0 \sim 10 M_E$, and small eccentricities, $e \approx 10^{-3}$, reach runaway growth on timescales of 20–40 Myr with 80 m initial bodies, 50–100 Myr with 800 m bodies, and 75–250 Myr for 8 km initial bodies. These growth times vary linearly with the mass of the annulus, $\tau_r \propto M_0^{-1}$, but are less sensitive to the initial eccentricity than constant-velocity models. In both sets of models, the timescales to produce 1000+ km objects are comparable to estimated formation timescales for Neptune. Thus, Pluto-sized objects can form in the outer solar system in parallel with the condensation of the outermost large planets.

Key words: Kuiper belt objects

1. INTRODUCTION

Current models for planetary formation involve aggregation of solid planetesimals and gas accretion in a circumstellar disk (e.g., Hayashi, Nakazawa, & Nakagawa 1985; Boss 1993; references therein). Large dust grains within the disk first settle to the midplane. These grains may then coagulate into successively larger grains (see, e.g., Weidenschilling 1980; Weidenschilling & Cuzzi 1985) or continue to settle in a very thin layer that eventually becomes gravitationally unstable (see, e.g., Goldreich & Ward 1973). Both paths produce kilometer-sized planetesimals that collide and merge to produce large bodies such as planets. Despite the complex and sometimes unknown physics, many simulations produce objects resembling known planets on timescales roughly comparable to the expected lifetime of the protosolar nebula (e.g., Safronov 1969; Greenberg et al. 1978, 1984; Nakagawa et al. 1983; Wetherill & Stewart 1989, 1993; Spaute et al. 1991; Kolvoord & Greenberg 1992; Weidenschilling & Davis 1992; Pollack et al. 1996).

Recent observations of slow-moving objects in the outer solar system offer a new challenge to planetary formation models. The trans-Neptunian region is now known to contain several dozen Kuiper Belt objects (KBOs) with estimated radii of 100–300 km (Jewitt, Luu, & Chen 1996). The orbits of known KBOs suggest a division into at least three dynamical components with an inner radius of 30 AU and an unknown outer radius: (1) the classical KBOs, objects with roughly circular orbits, (2) the resonant KBOs, objects in orbital resonance with Neptune (Jewitt et al. 1996), and (3) the scattered KBOs, objects with large, eccentric orbits (Luu et al. 1997). Although the known population is still small, Jewitt et al. (1996) estimate that the region between 30 and 50 AU contains $\approx 70{,}000$ objects larger than 100 km. The total mass in the classical Kuiper Belt is thus at least $0.1 M_E$. This mass probably represents a small fraction of the initial mass, because dynamical interactions with Neptune reduce the number of KBOs on short timescales compared with the age of the solar system (Levison & Duncan 1993; Malhotra 1996).

Despite these new observations, the origin of KBOs remains uncertain. Edgeworth (1949) and Kuiper (1951) first suggested that the Kuiper Belt was a natural extension of the original solar nebula. Holman & Wisdom (1993) later showed that small KBOs, once formed, can survive at 30–50 AU for times approaching the age of the solar system. More recent dynamical studies confirm this conclusion and explain the observed distribution of KBOs in a general way (Levison & Duncan 1993). The formation process and timescale for KBOs, however, is still controversial. Planetesimal simulations for plausible protosolar nebulae at 25–30 AU show that Neptune can grow to its present size in 10–100 Myr (Fernández & Ip 1981, 1984; Ip 1989; Pollack et al. 1996). These results suggest that Pluto

might form on a similar timescale at ~ 40 AU, because growth times are not a steep function of semimajor axis (see Aarseth, Lin, & Palmer 1993; Pollack et al. 1996; references therein). Nevertheless, Stern (1995, 1996) and Stern & Colwell (1997a, 1997b) conclude that KBO formation requires 100–1000 Myr for the conditions expected in the outer solar system. These limits far exceed the timescale required to produce Neptune, whose accretion time is constrained by the 10–100 Myr lifetime of the protosolar nebula (see Pollack et al. 1996 and references therein).

In this paper, we attempt to resolve the uncertainties surrounding KBO production with a new planetesimal simulation at 35 AU. We have developed an evolution code to follow the growth and velocity evolution of planetesimals with a wide range of initial masses. The code matches analytic models and duplicates Wetherill & Stewart's (1993, hereafter WS93) simulation of planetesimal evolution at 1 AU. Our numerical results demonstrate that small bodies with initial radii of 80 m to 8 km can produce $1000+$ km objects on timescales of 10–100 Myr. We confirm these calculations with a simple analytic estimate of the growth time as a function of semimajor axis. This analysis supports previous estimates of a short growth phase for Neptune, 10–100 Myr, and indicates that Pluto-Charon can form just outside the current orbit of Neptune on a similar timescale.

We outline the accretion model in § 2, describe our calculations in § 3, and conclude with a discussion and summary in § 4. The Appendix contains a complete description of the algorithms and detailed comparisons with analytic models.

2. ACCRETION MODEL

For our simulations of accretion in the Kuiper Belt, we adopt Safronov's (1969) particle-in-a-box method, in which planetesimals are treated as a statistical ensemble of masses with a distribution of horizontal and vertical velocities about a Keplerian orbit. Our simulations begin with a differential mass distribution, $n(m_i)$, in a single accumulation zone centered at a heliocentric distance a, with an inner radius at $a - \frac{1}{2}\Delta a$ and an outer radius at $a + \frac{1}{2}\Delta a$. We approximate the continuous distribution of particle masses with discrete batches having particle populations $n_i(t)$ and total masses $M_i(t)$ (WS93). The average mass of a batch, $m_i(t) = M_i(t)/n_i(t)$, changes with time as collisions add and remove bodies from the batch. This procedure naturally conserves mass and allows a coarser grid than simulations with fixed mass bins (Wetherill 1990 and references therein; WS93).

To evolve the mass and velocity distributions in time, we solve the coagulation and energy conservation equations for an ensemble of objects with masses ranging from $\sim 10^{12}$ to $\sim 10^{26}$ g. The Appendix describes our model in detail and compares our numerical results with analytic solutions for standard test cases. We adopt analytic cross sections to derive collision rates and compute velocity changes from gas drag and collective interactions such as dynamical friction and viscous stirring. Our initial approach to this problem ignores fragmentation, which we will consider in a later paper. In this study, we focus on developing a good understanding of planetesimal growth as a function of initial conditions in the Kuiper Belt.

To test our numerical procedures in detail, we attempt to duplicate WS93's simulations of planetary embryo formation at 1 AU. WS93 (see also Wetherill & Stewart 1989; Barge & Pellat 1990, 1991, 1993; Spaute et al. 1991; Aarseth et al. 1993) demonstrated that an ensemble of 8 km objects can produce 10^{26} g (Moon sized) objects on a 10^5 yr timescale. WS93's model begins with 8.33×10^8 planetesimals having radii of 8 km and a velocity dispersion of 4.7 m s^{-1} relative to a Keplerian orbit (Table 1; see also Table 1 of WS93). Tables 2 and 3 summarize our results using the WS93 initial conditions with mass-spacing factors of $\delta \equiv m_{i+1}/m_i = 1.25$ and 1.4 between successive mass batches and two different analytic cross sections. Figure 1 shows our reproduction of the WS93 results without fragmentation for

TABLE 1
BASIC MODEL PARAMETERS

Parameter	Symbol	1 AU Models	35 AU Models
Width of annulus (AU)	δa	0.17	6
Initial velocity (m s^{-1})	V_0	4.7	4.5–45
Particle mass density (g cm^{-3})......	ρ_0	3	1.5
Relative gas velocity (m s^{-1})	η	60	30
Time step (yr)	δt	0.5	5–250
Number of mass bins	N	100–150	64–128
Mass spacing of bins.................	δ	≤ 1.20	1.40

TABLE 2
MODEL RESULTS AT 1 AU

TIME (yr)	$\delta = 1.25$			$\delta = 1.40$		
	r_{max} (km)	$m(r_{max})$ (kg)	$N(r_{max})$	r_{max} (km)	$m(r_{max})$ (kg)	$N(r_{max})$
5.0×10^2......	19.8	9.7×10^{19}	3	20.9	1.2×10^{20}	1
1.0×10^4......	513.3	1.7×10^{24}	3	492.3	1.5×10^{24}	1
2.5×10^4......	1167.3	2.0×10^{25}	1	1203.0	2.2×10^{25}	1
5.0×10^4......	1540.8	4.6×10^{25}	3	1515.7	4.4×10^{25}	1
1.0×10^5......	1890.8	8.5×10^{25}	2	1746.7	6.7×10^{25}	3
1.5×10^5......	1948.3	9.3×10^{25}	5	2382.7	1.7×10^{26}	1

NOTE.—These results are for the Wetherill & Stewart 1993 prescription of gravitational focusing, eqs. (A12)–(A14), as summarized in the main text.

TABLE 3

MODEL RESULTS AT 1 AU

TIME (yr)	δ = 1.25			δ = 1.40		
	r_{max} (km)	$m(r_{max})$ (kg)	$N(r_{max})$	r_{max} (km)	$m(r_{max})$ (kg)	$N(r_{max})$
5.0×10^2......	19.8	9.7×10^{19}	3	20.9	1.2×10^{20}	1
1.0×10^4......	550.8	2.1×10^{24}	2	492.3	1.5×10^{24}	1
2.5×10^4......	1167.5	2.0×10^{25}	1	1223.0	2.3×10^{25}	1
5.0×10^4......	1458.6	3.9×10^{25}	4	1735.0	6.6×10^{25}	2
1.0×10^5......	1969.0	9.6×10^{25}	1	2174.8	1.3×10^{26}	1
1.5×10^5......	2121.0	1.2×10^{26}	1	2335.0	1.7×10^{26}	1

NOTE.—These results are for an adaptation of the Spaute et al. 1991 prescription of gravitational focusing, eq. (A16), as summarized in the main text.

$\delta = 1.25$. This simulation produces 14 objects of mass $(3-9) \times 10^{25}$ g in 1.5×10^5 yr, which agrees with the results in WS93 (see their Fig. 12). Our simulation confirms the broad "plateau" in the cumulative number, N_C, at $\log m_i = 24-26$ and the rough power-law dependence, $N_C \propto m_i^{-1}$, at $\log m_i = 21-23$. The broad plateau extends across a smaller mass range and becomes more rounded as δ increases (Fig. 2). The maximum planetesimal mass, m_{max}, at the conclusion of the calculation depends on both δ and the cross sections. We find marginally larger m_{max} for the Spaute et al. (1991) cross sections. In general, m_{max} increases as δ increases.

The evolution of particle velocities in our simulations agrees with the WS93 results (Fig. 1b). All of the velocities increase monotonically with time as a result of viscous stirring. The velocities of the larger bodies increase very slowly, because dynamical friction transfers their kinetic energy to the smaller bodies. The simulation maintains a nearly constant ratio of vertical to horizontal velocity, $v_i/h_i \approx 0.53$, for all but the most massive bodies, which have $v_i/h_i < 0.5$. The

equilibrium ratio of v_i/h_i yields $\langle i \rangle / \langle e \rangle \approx 0.6$, in agreement with Barge & Pellat (1990, 1991; see also Hornung, Pellat, & Barge 1985). At the conclusion of the simulation, our velocities for small bodies, $h_i \approx 500$ m s^{-1} at $m_i \sim 10^{19}$ g, are roughly 50% higher than those of WS93. Our velocities for large bodies, $h_i \approx 10$ m s^{-1} at $m_i \sim 10^{26}$ g, are roughly 50% lower than those of WS93. We also fail to reproduce WS93's abrupt drop in h_i at $\log m_i = 24$. However, these differences—which are independent of δ—have a negligible effect on the final mass distribution and probably result from slightly different algorithms for low-velocity collisions.

Gas drag is included in our simulations but has a negligible impact on the evolution. All of the 1 AU models lose $\sim 0.01\%$ of their initial mass over 1.5×10^5 yr. Velocity changes due to gas drag are essentially zero because the particle masses are so large.

To understand the sensitivity of these results to initial conditions, we consider the growth time of planetesimals from the coagulation equation (eq. [A3]). For most cases of interest, the growth time for bodies with m_i is approximately
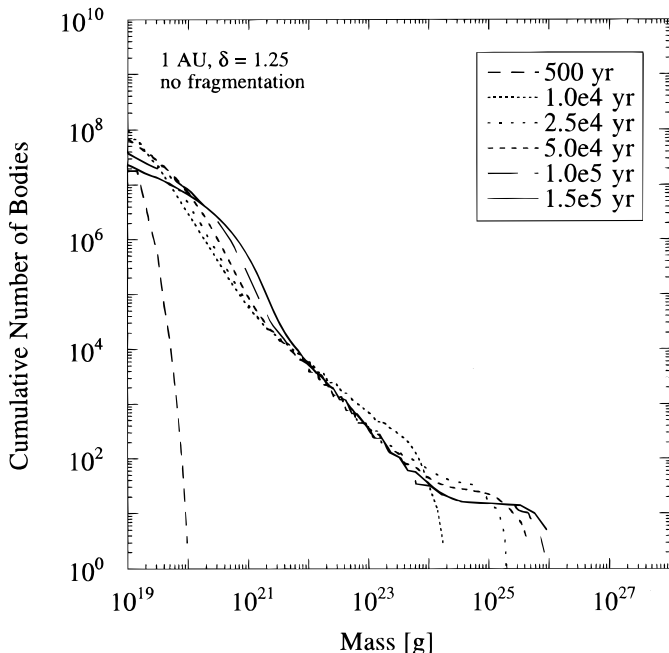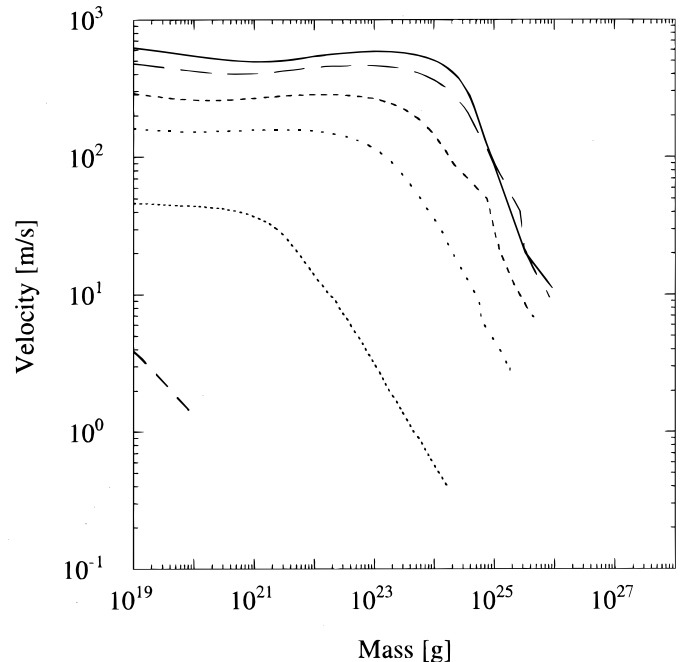

FIG. 1a

FIG. 1b

FIG. 1.—Results at 1 AU for $M_0 = 0.667 M_E$ and $\delta = 1.25$. (a) Cumulative mass distribution at selected times. The "runaway plateau" forms at $\sim 2 \times 10^4$ yr; it includes 17% of the total mass at 5×10^4 yr, 18% of the total mass at 10^5 yr, and 22% at 1.5×10^5 yr. (b) Horizontal velocity distribution. Viscous stirring increases all velocities with time; dynamical friction brakes the runaway bodies and increases the velocities of the lowest mass bodies.
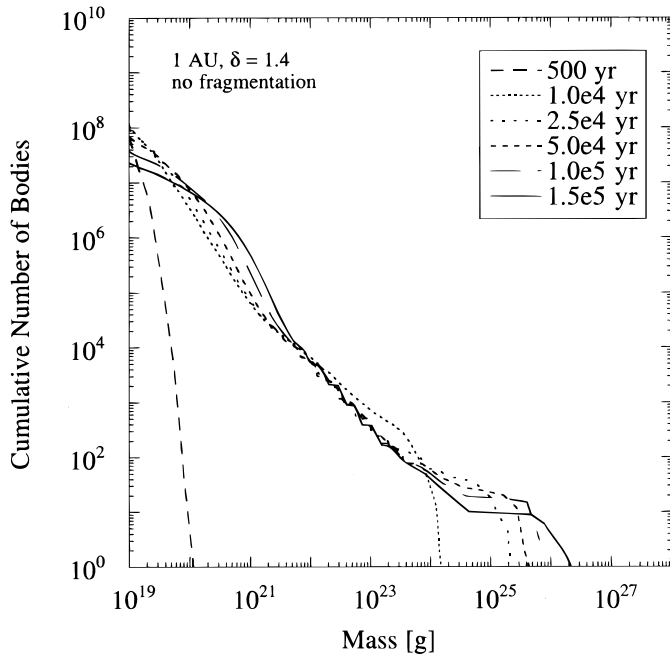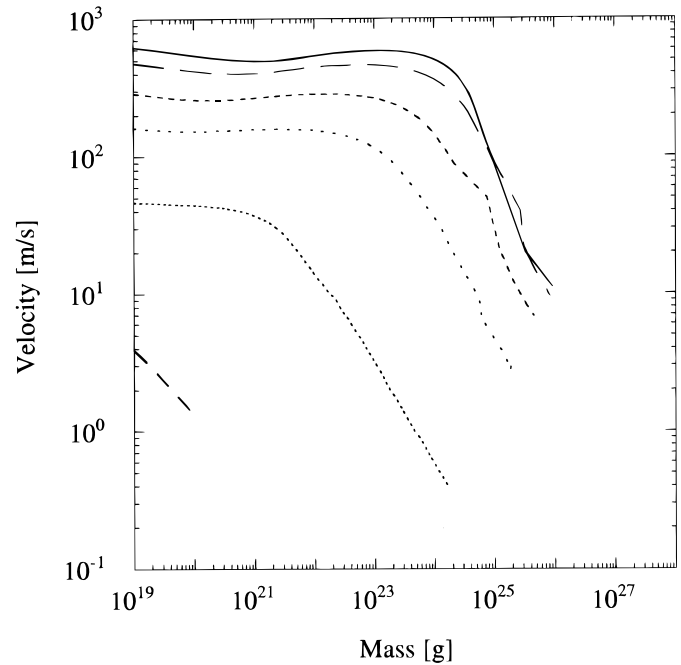
FIG. 2a

FIG. 2b

FIG. 2.—Results at 1 AU for $\delta = 1.4$. The runaway plateau is more poorly resolved as the mass spacing increases. (a) Cumulative mass distribution at selected times. The "runaway plateau" includes 12% of the total mass at 5×10^4 yr; this component comprises 18% of the total mass at 10^5 yr and 22% at 1.5×10^5 yr. (b) Horizontal velocity distribution. The horizontal velocities of low-mass objects are 5% larger with $\delta = 1.4$ than with $\delta = 1.25$. Higher mass bodies have velocities 2–3 times larger than comparable masses in $\delta = 1.25$ simulations.

$\tau \approx n_0/(dn/dt) \propto Ha\Delta a/n_j V F_g (r_i + r_j)^2$, where n_j is the number of lower mass bodies, V is the relative velocity, F_g is the gravitational focusing factor, r_i and r_j are the radii of particles i and j, and H is the vertical scale height. Collisions between low-mass objects are in the high-velocity regime, where the gravitational focusing factor is $F_g \approx 1$ and $\tau \propto a^{5/2}\Delta a n_j^{-1}(r_i + r_j)^{-2}$. This growth time is independent of the initial e and i. Gravitational focusing becomes effective in low-velocity collisions of massive objects; the growth time then depends on the initial velocity and is $\tau \propto a^{5/2}\Delta a n_j^{-1}(r_i + r_j)^{-1}V^2$. The extreme sensitivity of the growth time to velocity is the reason low-velocity planetesimals experience runaway growth in our 1 AU simulations (Wetherill & Stewart 1989; Ida & Makino 1992a, 1992b; Kokubo & Ida 1996; see also WS93 and references therein). We adopt 1000 km as a useful reference radius and write the time for 8 km objects to produce 1000 km objects at 1 AU as

$$\tau \approx \tau_0 \left(\frac{a}{1 \text{ AU}}\right)^{5/2}\left(\frac{\Delta a}{0.17 \text{ AU}}\right)\left(\frac{\rho_0}{3 \text{ g cm}^{-3}}\right)^{1/3}$$

$$\times \left(\frac{V_0}{450 \text{ cm s}^{-1}}\right)^2\left(\frac{6 \times 10^{27} \text{ g}}{M_0}\right) \qquad (1)$$

(see also Barge & Pellat 1990). Using our simulations with $\delta = 1.4$, we derive the proportionality constant for this standard case with velocity evolution, $\tau_{0,v} = 10,700$ yr, and for a model with no velocity evolution, $\tau_{0,nv} = 3750$ yr. Additional simulations confirm the mass, velocity, and volume dependence of this relation for factor of 2 variations in a, Δa, ρ_0, V_0, and M_0 about the values in equation (1) (see also Aarseth et al. 1993; Pollack et al. 1996).

3. KUIPER BELT CALCULATIONS

3.1. Starting Conditions

To choose appropriate constraints on planetesimal simu-

lations in the outer solar system, we rely on observations of other stellar systems and models of the protosolar nebula. First, current data indicate lifetimes of ~ 5–10 Myr for *typical* gaseous disks surrounding nearby pre–main-sequence stars and for the solar nebula (Sargent & Beckwith 1993; Strom, Edwards, & Skrutskie 1993; Russell et al. 1996). We adopt this estimate as a rough lower limit to the formation timescale of KBOs and assume that interactions between gas and planetesimals disappear on a similar time-scale, $\tau_g \approx 10$ Myr (see Appendix, eq. [A25]). Neptune formation places an upper limit on the KBO growth time, because Neptune excites KBOs through gravitational perturbations. Recent calculations suggest that Neptune can form in 5–100 Myr (Ip 1989; Lissauer & Stewart 1993; Lissauer et al. 1995). Once formed, Neptune inhibits KBO formation at 30–40 AU by increasing particle random velocities on timescales of 20–100 Myr (Holman & Wisdom 1993; Duncan, Levison, & Budd 1995). We thus adopt 100 Myr as a rough upper limit to the KBO formation timescale at 30–40 AU.

We assume a wide range of starting conditions for KBO simulations. Our model annulus is centered outside the orbit of Neptune at 35 AU and has a width of 6 AU. This annulus can accommodate at least 10–100 isolated bodies[1] with $m_i \gtrsim 10^{24}$ g for $e \leq 0.01$. The simulations begin with N_0 bodies of radius r_0, with $r_0 = 80$ m, 800 m, and 8 km. These bodies have small initial eccentricities, $e \sim 10^{-3}$ to 10^{-2} (Malhotra 1995), and an equilibrium ratio of inclination to eccentricity, $\beta = \langle i \rangle/\langle e \rangle = 0.6$ (Barge & Pellat 1990, 1991, 1993). The mass density of each body is fixed at 1.5 g cm^{-3}. To set N_0, we extend the minimum-mass solar

---

[1] "Isolated bodies" are planetesimals that cannot collide with one another, as defined in the Appendix following eq. (A4)

nebula to the Kuiper Belt and integrate the surface density distribution for solid particles, $\Sigma = \Sigma_0 (a/a_0)^{-3/2}$, across the 6 AU annulus. The dust mass is then $M_{min} \approx 0.25\Sigma_0 \, M_E$ at 32–38 AU ($a_0 = 1$ AU). Most minimum-mass solar nebula models have $\Sigma_0 = 30$–60 g cm^{-2}, which sets $M_{min} \approx (7$–$15)M_E$ (Weidenschilling 1977; Hayashi 1981; Bailey 1994). We thus consider models with initial masses of $M_0 = (1$–$100)M_E$ to allow for additional uncertainty in Σ_0. Table 1 compares input parameters for all Kuiper Belt models with initial conditions at 1 AU (see also WS93). Tables 4 and 5 summarize other initial conditions and results for the Kuiper Belt simulations summarized below.

Our success criteria are based on direct observations of KBOs. The present-day Kuiper Belt contains at least 70,000 objects with diameters exceeding 100 km at 30–50 AU (Jewitt & Luu 1995; Jewitt et al. 1996). This population is some fraction of the initial Kuiper Belt population, because Neptune has eroded the Kuiper Belt over time (Holman & Wisdom 1993; Duncan et al. 1995). Thus, a successful KBO simulation must achieve $r_5 \gtrsim 50$ km in $\lesssim 100$ Myr, where r_5 is the radius at which the cumulative number of objects N_C exceeds 10^5. Pluto formation is our second success criterion: plausible models must produce one or more objects with maximum radius $r_{max} \geq 1000$ km. In models with velocity evolution, we end simulations at 100–200 Myr or when r_{max} exceeds ~ 1000 km. To evaluate the dependence of runaway growth on the initial conditions, we extend

simulations without velocity evolution to 5000 Myr or to when r_{max} exceeds ~ 2000 km.

3.2. Models without Velocity Evolution

To isolate important processes in trans-Neptunian planetesimal evolution, we begin with constant-velocity solutions to the coagulation equation. We ignore fragmentation and fix the velocities for all masses at $h_i = 4.0 e_{init}$ km s^{-1} and $v_i = 3.6 \sin i_{init}$ km s^{-1}. The initial eccentricity and inclination are set at $i_{init} = 0.60 e_{init}$. The total mass and kinetic energy remain constant throughout the calculation. We also adopt a coarse mass-spacing factor, $\delta = 1.4$. This choice limits our ability to follow runaway growth with high accuracy during the late stages of the simulation but allows us to investigate a wide range of initial masses and velocities with a modest investment of computer time. Finally, we adopt simple formulae for gravitational focusing to speed our calculations (see eq. [A16]; Spaute et al. 1991). Table 4 summarizes the initial conditions and results for models with $M_0 = (1$–$100)M_E$ and $e_{init} = 10^{-3}$ and 10^{-2}.

Figure 3 shows how N_C evolves with time for a model with an initial planetesimal radius $r_0 = 8$ km, total mass $M_0 = 10M_E$, and $e_{init} = 10^{-3}$. This model begins with 1.87×10^{10} initial bodies and produces $\sim 42,500$ objects with twice the initial mass after $\tau = 100$ yr. Roughly half the original population experiences at least one collision by $\tau \approx 16$ Myr, when the 17 largest bodies have $m_i \approx 10^{20}$ g.

TABLE 4

MODEL RESULTS AT 100 Myr (NO FRAGMENTATION, NO VELOCITY EVOLUTION)

M_0 (M_E)	N_0	$r_{95\%}$ (km)	r_5 (km)	r_{max} (km)	$N(r_{max})$	τ_r (Myr)
$e = 10^{-3}$, $r_0 = 80$ m:						
1	1.87×10^{15}	0.5	0.6	0.9	1	2698
3	5.61×10^{15}	1.1	1.5	2.2	1	902
10	1.87×10^{16}	3.9	5.4	6.7	1925	270
30	5.61×10^{16}	...	...	8500	1	90
100......	1.87×10^{17}	...	...	18500	1	27
$e = 10^{-3}$, $r_0 = 800$ m:						
1	1.87×10^{12}	1.4	2.2	2.7	1	2340
3	5.61×10^{12}	2.2	3.0	4.2	4	780
10	1.87×10^{13}	5.5	8.5	10.7	341	234
30	5.61×10^{13}	...	...	18000	2	78
100......	1.87×10^{14}	...	...	16700	1	23.5
$e = 10^{-3}$, $r_0 = 8000$ m:						
1	1.87×10^{9}	13.3	16.9	20.7	140	753
3	5.61×10^{9}	19.2	26.8	36.7	91	250
10	1.87×10^{10}	...	...	7585	5	75
30	5.61×10^{10}	...	...	9800	1	25
100......	1.87×10^{11}	...	...	8700	2	7.5
$e = 10^{-2}$, $r_0 = 80$ m:						
1	1.87×10^{15}	0.5	0.6	0.9	1	...
3	5.61×10^{15}	1.1	1.5	1.9	634	...
10	1.87×10^{16}	3.1	4.8	6.0	28	2552
30	5.61×10^{16}	9.6	13.2	16.4	323	850
100......	1.87×10^{17}	33.6	46.5	63.5	5	255
$e = 10^{-2}$, $r_0 = 800$ m:						
1	1.87×10^{12}	1.4	2.2	2.4	3195	...
3	5.61×10^{12}	2.2	3.1	3.8	75	...
10	1.87×10^{13}	4.4	6.8	7.4	2018	2521
30	5.61×10^{13}	10.8	14.8	18.4	387	840
100......	1.87×10^{14}	37.6	51.8	65.0	70	251
$e = 10^{-2}$, $r_0 = 8000$ m:						
1	1.87×10^{9}	10.1	11.6	16.1	1	...
3	5.61×10^{9}	11.7	14.9	18.5	8	...
10	1.87×10^{10}	13.4	18.5	23.3	298	2146
30	5.61×10^{10}	21.2	29.3	39.9	1	716
100......	1.87×10^{11}	59.2	81.9	104.2	18	215

TABLE 5
MODEL RESULTS (VELOCITY EVOLUTION, NO FRAGMENTATION)

M_0 (M_E)	N_0	$r_{95\%}$ (km)	r_5 (km)	r_{max} (km)	$N(r_{max})$	τ_r (Myr)
$e = 10^{-3}, r_0 = 80$ m:						
1	1.87×10^{15}	0.5	0.8	0.9	6	...
2	3.74×10^{15}	2.6	30.4	126.1	2	...
3	5.61×10^{15}	2.7	33.8	603.4	1	184
6	1.12×10^{16}	2.9	44.1	1072.6	1	67
10	1.87×10^{16}	2.6	54.1	1000.5	1	32
17	3.18×10^{16}	2.4	55.7	1008.5	1	18
30	5.61×10^{16}	2.7	74.4	1059.2	1	10
$e = 10^{-3}, r_0 = 800$ m:						
1	1.87×10^{12}	1.4	2.3	2.7	9	...
2	3.74×10^{12}	2.0	3.2	3.7	24	...
3	5.61×10^{12}	2.8	5.4	6.8	1	...
6	1.12×10^{13}	11.2	47.3	456.9	1	155
10	1.87×10^{13}	10.6	51.4	1007.8	1	83
17	3.18×10^{13}	10.6	68.2	1022.7	1	46
30	5.61×10^{13}	10.6	90.7	1000.3	2	25
$e = 10^{-3}, r_0 = 8000$ m:						
1	1.87×10^{9}	11.7	17.9	23.9	8	...
2	3.74×10^{9}	15.3	24.1	32.7	7	...
3	5.61×10^{9}	17.3	30.6	46.0	4	...
6	1.12×10^{10}	27.3	57.1	123.0	1	...
10	1.87×10^{10}	43.4	90.6	462.4	1	132
17	3.18×10^{10}	48.8	101.2	1050.0	1	76
30	5.61×10^{10}	51.7	114.2	1017.7	2	44
$e = 10^{-2}, r_0 = 80$ m:						
1	1.87×10^{15}	0.4	0.6	0.8	762	...
2	3.74×10^{15}	0.7	1.2	1.4	39	...
3	5.61×10^{15}	1.0	1.8	1.9	1103	...
6	1.12×10^{16}	5.8	46.6	294.7	1	126
10	1.87×10^{16}	6.3	60.4	1004.1	1	76
17	3.18×10^{16}	6.4	70.0	1002.2	2	43
30	5.61×10^{16}	6.4	82.2	1070.2	1	24
$e = 10^{-2}, r_0 = 800$ m:						
1	1.87×10^{12}	1.4	2.2	2.7	2	...
2	3.74×10^{12}	1.8	2.8	3.4	2	...
3	5.61×10^{12}	2.2	3.3	3.8	48	...
6	1.12×10^{13}	3.1	4.9	6.0	1	...
10	1.87×10^{13}	4.4	7.3	8.4	78	...
17	3.18×10^{13}	13.9	43.0	74.1	4	130
30	5.61×10^{13}	23.4	90.8	1000.5	2	73
$e = 10^{-2}, r_0 = 8000$ m:						
1	1.87×10^{9}	10.1	13.0	16.3	6	...
2	3.74×10^{9}	10.1	14.3	16.4	303	...
3	5.61×10^{9}	11.7	15.3	18.3	11	...
6	1.12×10^{10}	13.2	17.8	20.7	68	...
10	1.87×10^{10}	13.4	20.8	26.1	2	...
17	3.18×10^{10}	17.0	25.9	31.0	46	...
30	5.61×10^{10}	28.3	45.8	62.3	6	167

Slow growth continues until $\tau \approx 59$ Myr, when the three largest objects have sizes comparable to large KBOs, $r_i \approx 100$ km and $m_i \approx 10^{22}$ g. The growth rate of the large masses then increases considerably because of gravitational focusing. Runaway growth ensues. The cumulative mass distribution then follows a power law, $N_C \propto r_i^{-2.75}$, at low masses and develops a high-mass shoulder that extends to larger and larger masses as the simulation proceeds. This shoulder resembles the runaway plateau observed in 1 AU models but does not evolve into a true plateau with $N_C \approx$ const as in Figures 1 and 2. The largest planetesimals reach $r_{max} \approx 200$ km at $\tau \approx 66$ Myr; r_{max} exceeds 1000 km only 9 Myr later. A single runaway body with $r_{max} \approx 4000$ km begins to sweep up lower mass planetesimals at $\tau \approx 80$ Myr; by $\tau \approx 85$ Myr, it contains essentially all of the mass in the annulus.

Simulations with $r_0 = 8$ km produce runaway growth independent of the initial mass in the annulus. Figure 4a

indicates that each model experiences a long, linear growth phase until $r_{max} \approx 100$–200 km. The largest objects then begin a short rapid-growth phase that produces several isolated, runaway bodies with $r_{max} \approx 1000$ km. These runaway bodies accumulate all of the lower mass bodies and may merge to form a single runaway body if the isolation criterion permits. The time to produce runaway bodies with $r_i = 1000$ km scales with the mass in the annulus, $\tau_r \approx 753(M_0/M_E)^{-1}$ Myr. For comparison, our scaling relation in equation (1) predicts $\tau_r \approx 775(M_0/M_E)^{-1}$ Myr for $\rho_0 = 1.5$ g cm^{-3} in a 6 AU annulus centered at 35 AU.

Runaway growth also occurs independently of the initial radius, r_0 (Figs. 4a–4c). Because of smaller initial cross sections, models with $r_0 = 80$–800 m take longer to reach the rapid-growth phase. These models make the transition from rapid growth to runaway growth more quickly, because it is easier for 100+ km objects to sweep up small objects with $r < 1$ km. In all cases, a single runaway body with $r > 1000$
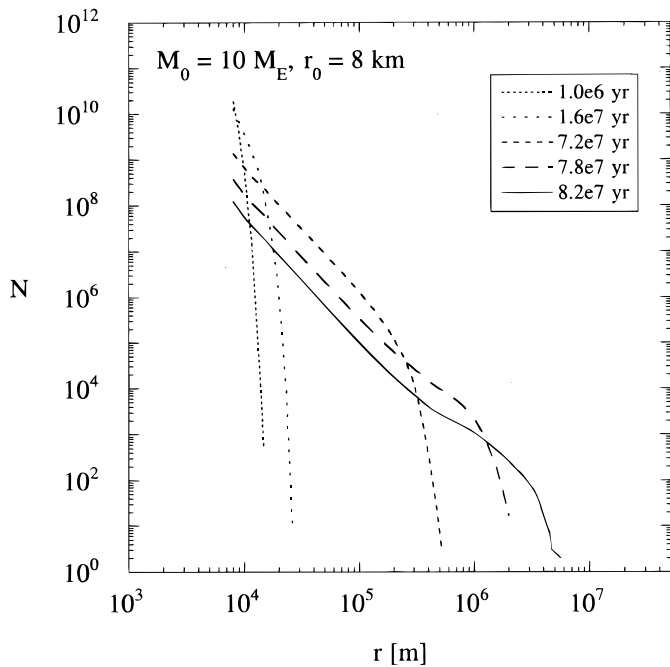
Fig. 3.—Cumulative size distribution for $M_0 = 10M_E$, $r_0 = 8$ km, and $e = 10^{-3}$. The eccentricity of this model is constant in time. Collisional growth is quasi-linear for 50 Myr until the largest bodies have $r_{max} = 50$ km. Runaway growth begins when $r_{max} \gtrsim 100$ km; these bodies then grow to sizes of 10^3 km to 10^4 km in 20–30 Myr.

km eventually accumulates all of the mass in each simulation, although the timescale is quite long, $\tau_r \approx 2700$ Myr, for simulations with $M_0 = M_E$ and $r_0 = 80$ m. Again, the runaway growth time scales with mass: $\tau_r \approx 2340(M_0/M_E)^{-1}$ Myr for $r_0 = 800$ m and $\tau_r \approx 2700(M_0/M_E)^{-1}$ Myr for $r_0 = 80$ m. The small increase in τ_r with initial radius for $r_0 \lesssim 800$ m suggests that models with $r_0 < 80$ m will reach runaway growth on timescales of ~ 3000 Myr, which is ~ 40 times slower than models with $r_0 = 8$ km.

Our results also confirm the velocity dependence derived in equation (1). Low-eccentricity simulations with 50% smaller initial velocities reach runaway growth in 25% of the time for our standard model; simulations with twice the initial velocity require 4 times as long to achieve runaway growth. This simple relation begins to break down as the eccentricity increases to $e \approx 10^{-2}$, as outlined below. The runaway time also scales with the width of the annulus, Δa, and the semimajor axis, a, as indicated in equation (1).

High-eccentricity models also achieve runaway growth but do not follow precisely the velocity scaling in equation (1). Figure 5 shows the radius evolution for models with different r_0 and m_0 for $e = 10^{-2}$ (see also Table 4). The growth time for 1000+ km objects is $\tau_r \approx 20–25(M_0/M_E)^{-1}$ Gyr, nearly independent of the initial radius and velocity. This relation contrasts with the low-eccentricity results, where the growth time is very sensitive to the initial conditions. In all our simulations, planetesimal growth is orderly until gravitational focusing becomes important and runaway growth occurs. However, the radius where gravitational focusing becomes important increases from $r_i \sim 10$ km at $e = 10^{-3}$ to $r_i \sim 100$ km at $e = 10^{-2}$. For models with small initial bodies, $r_0 \lesssim 800$ m, the timescale to reach runaway growth is directly proportional to e. For models

with large initial eccentricity, the long orderly phase also "erases" memory of the initial radius. Thus, τ_r is nearly independent of r_0 for large e. The relatively short orderly growth phase of low-e models does not erase memory of r_0; τ_r decreases with increasing r_0 for $e_{init} \lesssim 0.05$. For models with $r_0 \sim 8$ km, gravitational focusing accelerates growth immediately at low e. These simulations do not have an orderly growth phase; instead, they follow the 1 AU simulations and satisfy the scaling relation in equation (1).

Before we consider Kuiper Belt simulations with velocity evolution, our basic result that constant-velocity models achieve runaway growth deserves some comment. First, previous simulations at 1 AU show that runaway growth requires dynamical friction to decrease the velocities of the largest bodies to the regime where gravitational focusing becomes important (Wetherill & Stewart 1989, 1993; Barge & Pellat 1990, 1991; Ida 1990; Ida & Makino 1992a, 1992b; Ohtsuki 1992; Kokubo & Ida 1996). In Kuiper Belt models with $e_{init} = 10^{-3}$, gravitational focusing factors become very large at planetesimal masses of 10^{23} to 10^{24} g. Further growth of these bodies only enhances gravitational focusing, because the escape velocity increases while the impact velocities remain low. More massive objects thus "run away" from their lower mass counterparts. This response occurs in *any* constant-velocity simulation as long as bodies can reach masses at which the escape velocity is large compared with the relative impact velocity, $V_{e,ij}/V_{ij} \gg 1$. Models with $e_{init} \gtrsim 0.1$ never reach this limit for plausible M_0 and thus do not experience runaway growth. Models with $e_{init} \lesssim 0.05$ always produce runaway bodies, albeit at much later stages than models with $e_{init} \sim 10^{-3}$ (Fig. 5).

Our final comment on runaway growth concerns the shape of the cumulative number distribution near the end of the simulation. During runaway growth, models at 1 AU develop a plateau in the cumulative number distribution that extends from $m_i = 10^{23}$ g to $m_i = 10^{25}–10^{26}$ g (see Figs. 1 and 2). This plateau separates runaway bodies from the lower mass objects, which are in the orderly growth regime and have a power-law size distribution, $N_C \propto r_i^{-3}$ for log $m_i = 21–24$ (WS93; see Figs. 1–2). The Kuiper Belt simulations also produce a power-law size distribution, $N_C \propto r_i^{-2.7}$ for $m_i \lesssim 10^{25}$ g, but they develop a high-mass "shoulder" instead of a marked plateau at runaway growth (see Fig. 3). To test whether this feature is a function of the mass resolution as in 1 AU models, we simulated evolution at 35 AU with $\delta = 1.1$ and 1.25 for $M_0 = 10M_E$ and $r_0 = 8$ km. As the mass resolution in the simulation increases from $\delta = 1.4$ to $\delta = 1.1$, the high-mass shoulder follows a very shallow power law, $N_C \propto r_i^{-1.7}$ (Fig. 6). This power law becomes better defined as the mass resolution increases further, but it never develops into the "runaway plateau" produced in the 1 AU models (Figs. 1–2). This result suggests that the broad plateau in 1 AU models is the result of velocity evolution, which reduces the velocity of the most massive objects and enhances gravitational focusing (WS93). We will now test this hypothesis by considering Kuiper Belt models with velocity evolution.

3.3. Models with Velocity Evolution

To understand the importance of velocity evolution in the Kuiper Belt, we add several physical processes to the calculation: (1) gas drag, (2) dynamical friction and viscous stirring from long-range (elastic) collisions, and (3) dynamical friction and viscous stirring from short-range (inelastic)
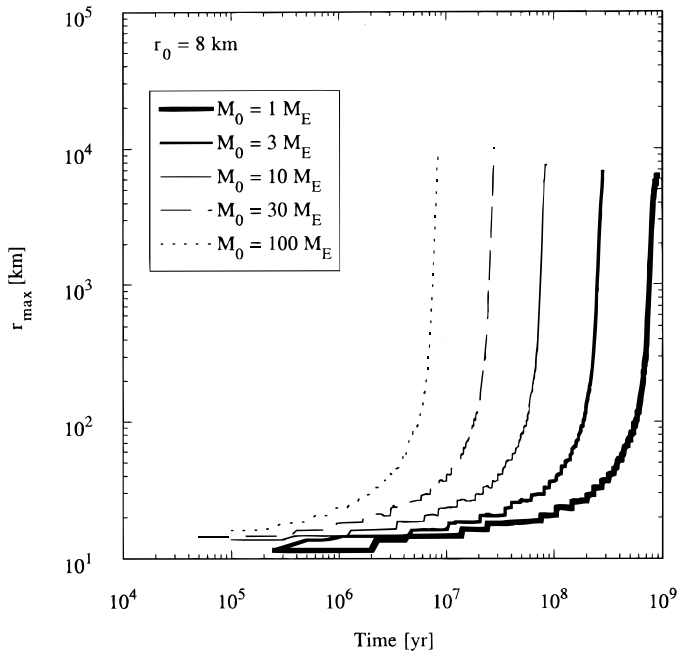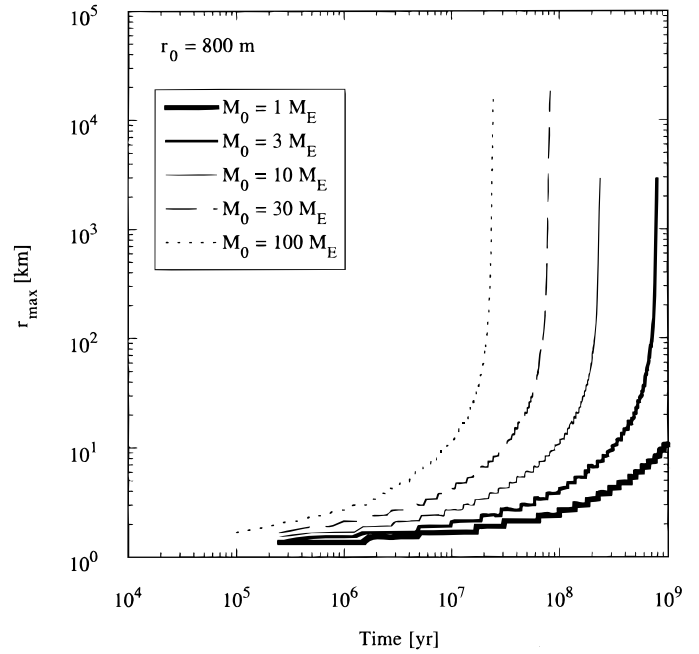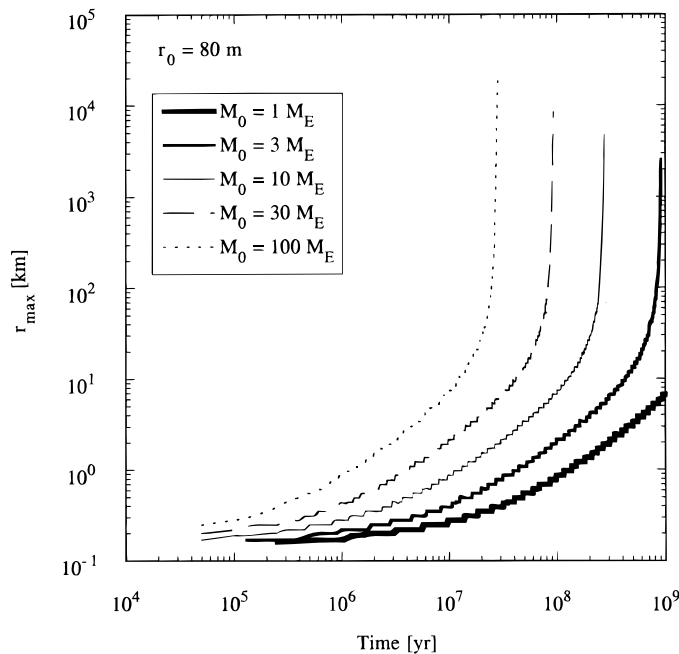
FIG. 4a

FIG. 4b

FIG. 4c

FIG. 4.—Radius evolution as a function of initial mass for constant-velocity models, with (a) $r_0 = 8$ km, (b) $r_0 = 800$ m, and (c) $r_0 = 80$ m. The eccentricity is $e = 10^{-3}$. The time to runaway growth scales inversely with initial mass, $\tau_r \approx \tau_0 (M_0/M_E)^{-1}$; $\tau_0 \approx 753$ Myr for $r_0 = 8$ km, $\tau_0 \approx 2340$ Myr for $r_0 = 800$ m, and $\tau_0 \approx 2700$ Myr for $r_0 = 80$ m.

collisions. As in our constant-velocity models, we begin with N_0 bodies at radii $r_0 = 80$ m, 800 m, and 8 km. We adopt $\delta = 1.4$ for the mass-spacing factor and use our simple expression for gravitational focusing, equation (A16). The initial velocities are $h_i = 4.0(e_{\rm init}/10^{-3})$ m s^{-1} and $v_i = 2.1(e_{\rm init}/10^{-3})$ m s^{-1}. The eccentricity and inclination evolve separately as a result of collisions and collective interactions (see Appendix, § A3). Table 5 summarizes the initial conditions and results for models with $M_0 = (1–30)M_E$ and $e_{\rm init} = 10^{-3}$ to 10^{-2}.

Before describing the results of our simulations, it is useful to compare various timescales for velocity evolution

at 35 AU. First, gas drag is negligible in models that ignore fragmentation. A typical simulation at 35 AU loses $\sim 10^{-5}$ % of its total mass as a result of gas drag in 100 Myr. Velocity changes due to gas drag are also insignificant; the timescale for gas drag to modify the velocity exceeds 10 Gyr for all masses in our simulation.

Velocity changes due to elastic and inelastic collisions, however, are significant. Figure 7a compares timescales, $\tau_{v,h} = h_i/(dh_i/dt)$, for horizontal velocity evolution as a function of particle mass at 35 AU. The two curves show $\tau_{v,h}$ for interactions between particles of the same mass with a power-law size distribution, $N_c \propto r^{-2.7}$, and constant
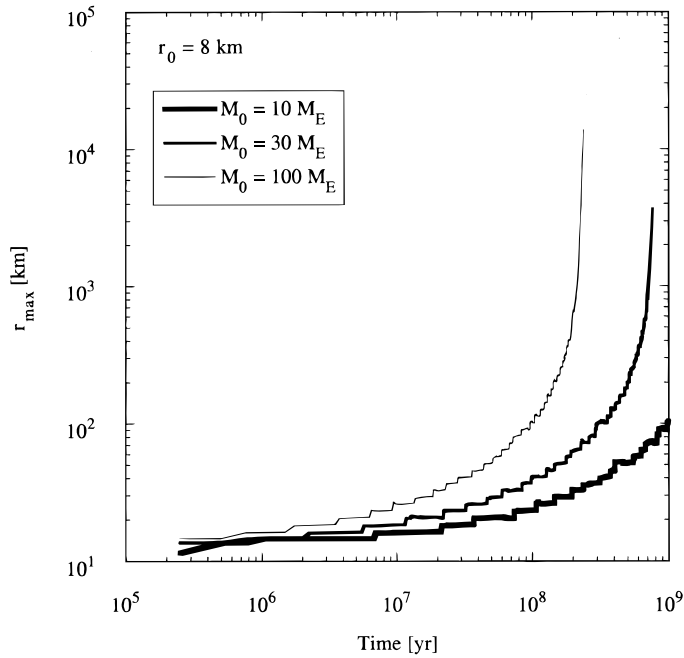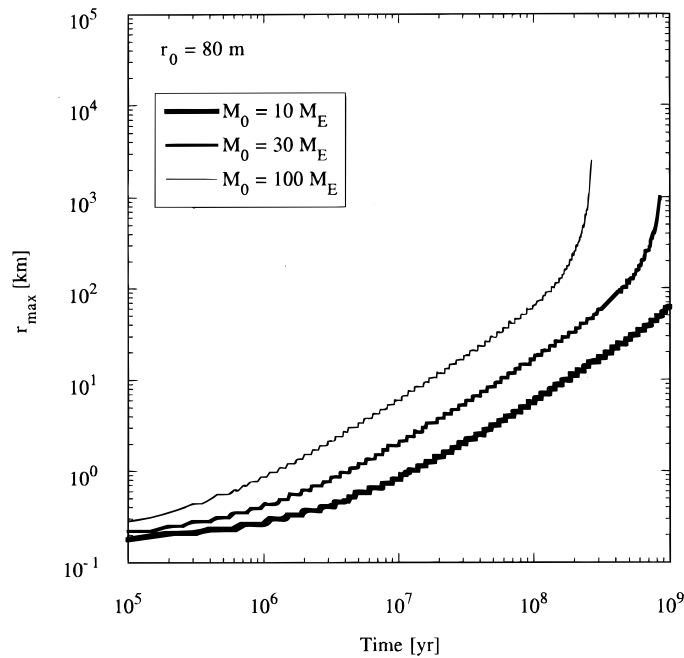
FIG. 5a
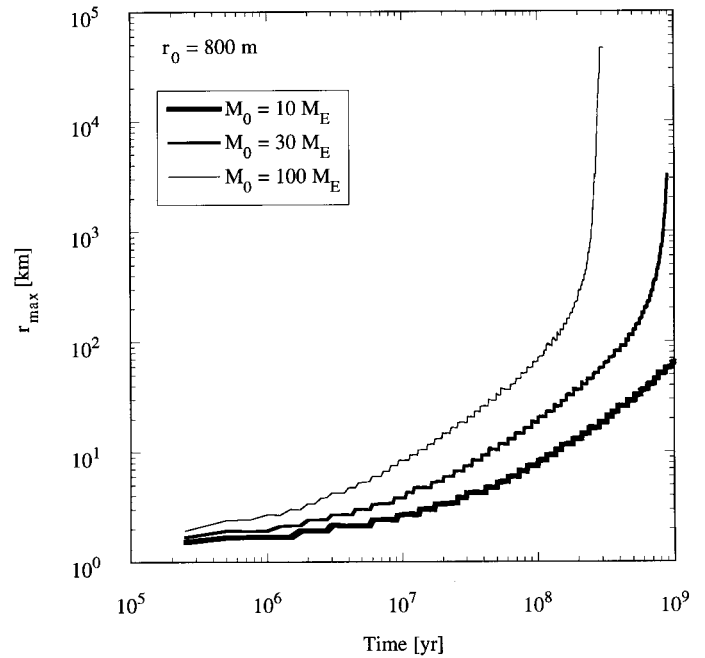
FIG. 5b

FIG. 5c

FIG. 5.—Same as Fig. 4, but with eccentricity $e = 10^{-2}$: $(a)\,r_0 = 8$ km, $(b)\,r_0 = 800$ m, and $(c)\,r_0 = 80$ m

velocity. These timescales are *not* integrated over the size distribution and are relevant only when a simulation has a small range of masses. Viscous stirring—which tends to increase particle velocities—is ineffective for $m_i \lesssim 10^{13}$ kg, $\tau_{v,h} \approx 10^{16}$ yr, but very effective, $\tau_{v,h} \lesssim 10^6$ yr, at $m_i \gtrsim 10^{17}$ kg. Collisional damping is also more effective at large masses, but the timescale is much less mass sensitive than viscous stirring. Collisional damping balances viscous stirring for an initial particle mass $m_0 \approx 10^{15}$ kg, which corresponds to $r_0 \approx 5$ km.

To illustrate these points in more detail, Figures 7b and 7c plot the *integrated* timescales, $\tau_{v,h} = \sum_{i=1}^{N} h_i/(dh_i/dt)$, for the horizontal velocity at two stages of a model with veloc-

ity evolution. In Figure 7b, the maximum mass has $m_{\max} \approx 10^{14}$ kg. Collisional damping still dominates viscous stirring for the lowest masses, but the mass at which the two processes balance has moved from $m_i \approx 10^{15}$ kg to $m_i \approx 5 \times 10^{11}$ kg. Once $m_{\max} \approx 10^{19}$ kg, viscous stirring dominates collisional damping for all masses. Particle velocities thus increase once massive objects with $r_i \gtrsim 100$ km are produced. The timescale for viscous stirring is quite short, $\lesssim 10^6$ yr, at the lowest masses considered in our models, so the velocity increases can be large during the 100 Myr timescale of a typical simulation.

Figure 8 shows how N_C and h_i evolve with time in a model with $r_0 = 8$ km, $M_0 = 10M_E$, and $e_{\text{init}} = 10^{-3}$. The
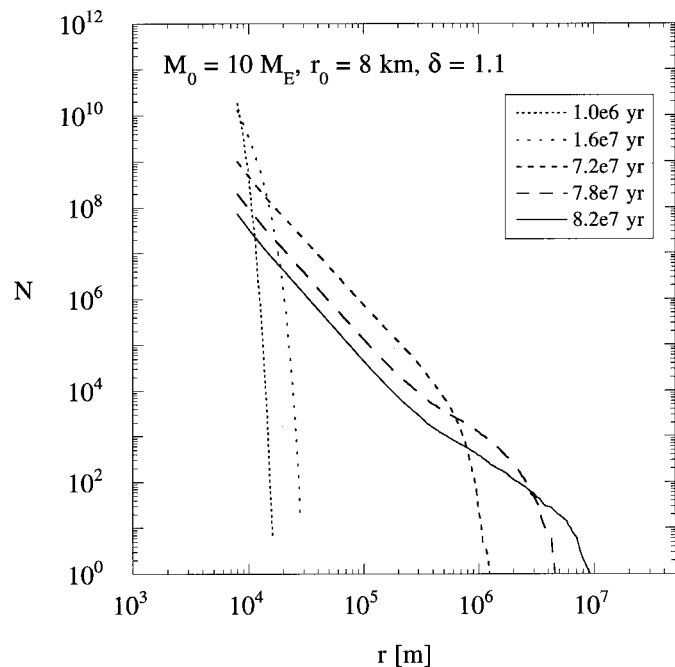
FIG. 6.—Cumulative size distribution for a constant-velocity model with $\delta = 1.1$ for $M_0 = 10 M_E$, $r_0 = 8$ km, and $e = 10^{-3}$. This model produces a cumulative size distribution with two distinct power laws: $N_C \propto r^{-2.7}$ for 8 km $\lesssim r_i \lesssim 300$ km and $N_C \propto r^{-1.7}$ for 300 km $\lesssim r_i \lesssim 5000$ km.

simulation begins with $N_0 = 1.87 \times 10^{10}$ and produces 762 objects having 8 times the initial mass in 1 Myr. Roughly half the initial bodies experience at least one collision by 24 Myr, when the largest object has $r_{max} \approx 37$ km. The horizontal velocities then range from $h_i = 1$ m s^{-1} at $r_i = 37$ km up to $h_i = 7$ m s^{-1} at $r_i = 8$ km. Orderly growth produces $r_i = 100$ km objects at 56 Myr, and this population reaches $N_C \approx 100$ at 61 Myr. This phase continues until ~ 100 Myr, when Charon-sized objects with $r_i \approx 500$ km begin to grow rapidly. There are 10 "Charons" at 110 Myr, 47 at 125 Myr, 107 at 150 Myr, and 202 at 180 Myr, when we ended the simulation. At 180 Myr, 20 Pluto-sized objects with $r_i \approx 1000$ km are isolated bodies about to run away from the rest of the mass distribution.

In contrast to the constant-velocity simulations with low e_{init}, this model does not immediately enter a rapid-growth phase once objects with $r_i \approx 100$ km are first produced. Viscous stirring and dynamical friction slowly increase the velocities of low-mass bodies throughout the simulation: the horizontal velocity increases from $h_{init} = 4$ m s^{-1} to $h_i \approx 65$ m s^{-1} at 180 Myr (Fig. 8). This 20-fold increase in the eccentricity reduces gravitational focusing by a factor of 400 and retards the growth of the most massive objects. Evolution thus proceeds at a pace between the constant-velocity simulations with $e_{init} = 10^{-3}$ and $e_{init} = 10^{-2}$.

The evolution for simulations with smaller initial masses is different, because collisional damping then dominates the velocity evolution (Fig. 7). Figure 9 shows the time evolution of N_C and h_i for $r_0 = 800$ m, $M_0 = 10 M_E$, and $e_{init} = 10^{-3}$. This simulation begins with $N_0 = 1.87 \times 10^{13}$ and produces five objects having 8 times the initial mass in 1 Myr. It takes only 7.7 Myr for half the initial objects to collide at least once. The maximum radius is then $r_{max} \approx 2.5$ km. Velocity damping from inelastic collisions overcomes viscous stirring, so the particle velocities remain low and do

not change significantly with mass. As evolution proceeds, dynamical friction efficiently damps the velocities of the largest bodies, but collisional damping still maintains modest velocities at low masses. Bodies with $r_i = 8$–10 km begin to form at 32–33 Myr, when only 11% of the original objects remain. The evolution soon overtakes the $r_0 = 8$ km model. Orderly growth produces 50 km objects at 45 Myr and 100 km objects at 48 Myr. Runaway growth begins shortly thereafter. Charon-sized objects form at 60 Myr and reach Pluto size at 80–81 Myr.

Simulations with $r_0 = 80$ m reach runaway growth on even faster timescales. Figure 10 shows the time evolution of N_C and h_i for $M_0 = 10 M_E$ and $e_{init} = 10^{-3}$. At 1 Myr, only 43% of the initial bodies have yet to experience a collision; 33 objects already have $r_i \approx 270$ m. The maximum radius reaches $r_{max} = 800$ m in 9 Myr and $r_{max} = 8$ km in 17 Myr. The low-mass bodies first lose $\sim 50\%$ of their initial velocity, $h_{init} = 4$ m s^{-1}, and begin to increase in velocity at 17–18 Myr, when viscous stirring from long-range collisions finally overcomes damping from inelastic collisions. At this time, the high-mass bodies have low velocities as a result of dynamical friction, $h_i \approx 0.01$ m s^{-1}, and begin to grow rapidly. A runaway plateau in the N_C distribution develops at 24 Myr and extends to Charon-sized objects at 25 Myr. At the conclusion of this simulation at 33 Myr, five Pluto-sized objects have $r_i \approx 900$–1000 km. The velocities of these high-mass objects are then $h_i \approx 0.03$–0.05 m s^{-1}.

With their long runaway growth times, models with $r_0 = 8$ km cannot meet both of our success criteria unless the initial mass is very large, $M_0 \gtrsim (15$–$20)M_E$. Viscous stirring and dynamical friction increase the velocities of the small objects throughout these simulations, which reduces gravitational focusing and delays runaway growth compared with models with smaller r_0. The long approach to runaway growth allows the production of many large KBOs; simulations with $M_0 \approx (6$–$20)M_E$ have $r_5 \approx 50$–100 km and thus reach our first success criterion. However, the timescale to produce $1000+$ km objects is 4–5 times longer than models with $r_0 = 80$ m, i.e., $\tau_r \approx 130(M_0/10M_E)^{-1}$ Myr. Most of these models thus fail to make Pluto on a reasonable timescale.

Models starting with lower mass objects, $r_0 = 80$ and 800 m, meet both success criteria. Although viscous stirring and dynamical friction stir up the velocities of the lowest mass objects, the timescale for the velocity to increase is large compared with models with $r_0 = 8$ km (see Fig. 7). The $r_0 = 800$ m models reach runaway growth faster than models with $r_0 = 8$ km and produce Pluto-sized objects in $\tau_r \approx 83(M_0/10M_E)^{-1}$ Myr for $e_{init} = 10^{-3}$. The combination of smaller particle velocities and a shorter time to runaway growth results in fewer KBOs compared with models with $r_0 = 8$ km (Fig. 11). Nevertheless, these models achieve $r_5 \approx 50$–90 km during the runaway growth phase.

Models with $r_0 = 80$ m and $e_{init} = 10^{-3}$ have the shortest runaway growth times and produce the fewest numbers of KBOs. The timescale to produce Pluto-sized planets is $\tau_r \approx 32(M_0/10M_E)^{-1}$ Myr for $e_{init} = 10^{-3}$, which easily allows Pluto formation in a minimum-mass solar nebula as Neptune forms at a smaller semimajor axis. These models, however, struggle to build a population of 10^5 KBOs during the runaway growth phase. With relatively low particle velocities at all masses (see Fig. 10b), objects with $r_i \approx 10$–20 km do not grow as rapidly as larger bodies. This evolution tends to concentrate material in the more massive
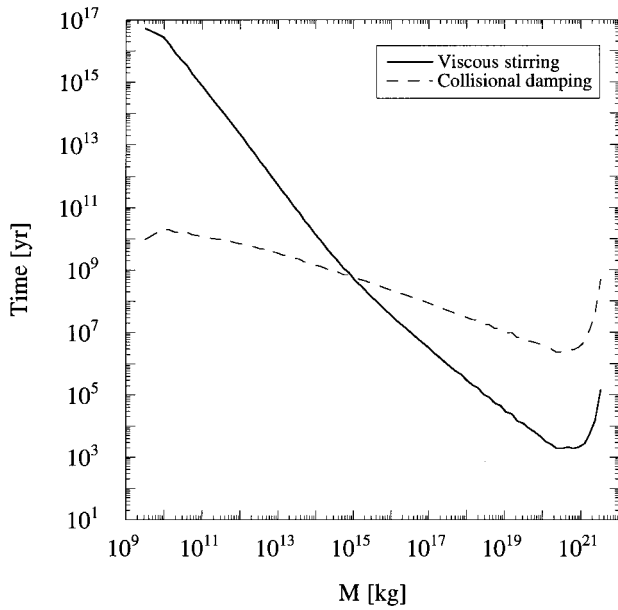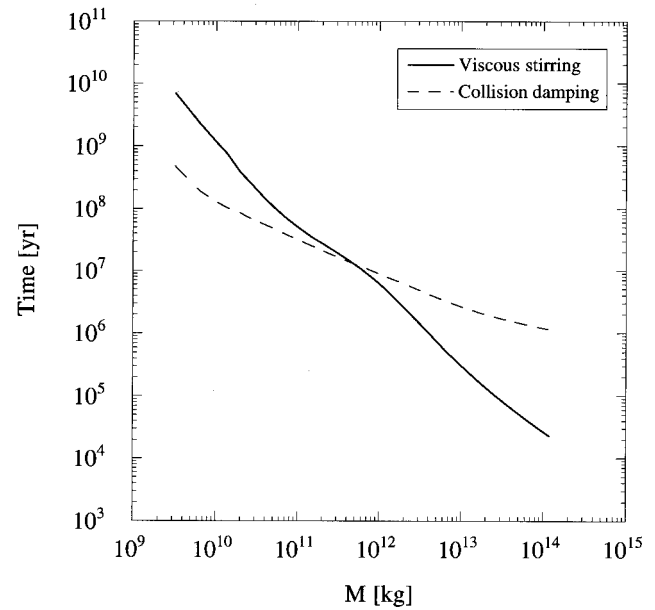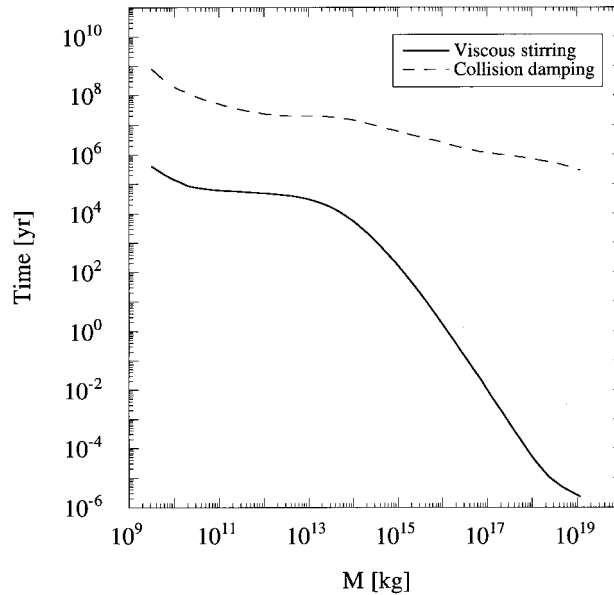
FIG. 7a

FIG. 7b

FIG. 7c

FIG. 7.—Timescales for viscous stirring (*solid curve*) and collisional damping (*dashed curve*) as a function of mass. (*a*) The two curves show the timescales for interactions only between particles of the same mass for a realistic cumulative mass distribution. The two plots curve up at high masses because of the small number of particles. Collisional damping balances the velocity increase due to viscous stirring at $\sim 10^{15}$ kg. (*b*) Timescales integrated over all particles during the initial stages, ~ 10 Myr, of a model with velocity evolution. Collisional damping overcomes velocity increases from viscous stirring only for $m_i \lesssim 10^{12}$ kg. (*c*) As in (*b*), but for a late stage in the growth process, 15–16 Myr. The integrated effects of viscous stirring now increase the velocities of all particles.

KBOs and reduces the number of lower mass KBOs with $r_i \approx 50$–100 km. This smaller r_5 in the calculations leads to partially successful models that yield several Pluto-sized objects and $r_5 \lesssim 50$ km (Table 5).

At large initial eccentricity, planetesimal growth follows the evolution of low-eccentricity models, but on longer timescales (Fig. 12). In simulations with $r_0 = 80$ and 800 m, there are enough small bodies for inelastic collisions to damp the particle velocities substantially. Dynamical friction further decreases the velocities of the most massive bodies and allows runaway growth to occur on reasonable timescales. In simulations with $r_0 = 80$ m and $e_{init} = 10^{-2}$, runaway growth is delayed by a factor of ~ 2.5 compared

with simulations with $e_{init} = 10^{-3}$. This delay increases to a factor of ~ 3 for $r_0 = 800$ m. At $r_0 = 8$ km, collisional damping initially reduces particle velocities but is overcome by viscous stirring when $r_{max} \approx 50$ km. At this time, the velocities are large, $V_i \approx 30$ m s^{-1}, and growth is slow. None of these models reach runaway growth on a 100 Myr timescale. Runaway growth, if it occurs, is delayed by a factor of ~ 6 in large-e_{init} models compared with that in low-e_{init} models.

Our results for large e_{init} thus favor low-mass initial bodies. Simulations with $r_0 = 80$ m and $e_{init} = 10^{-2}$ produce more KBOs with $r_i \approx 50$–100 km than their low-e_{init} counterparts. The longer orderly growth phase and
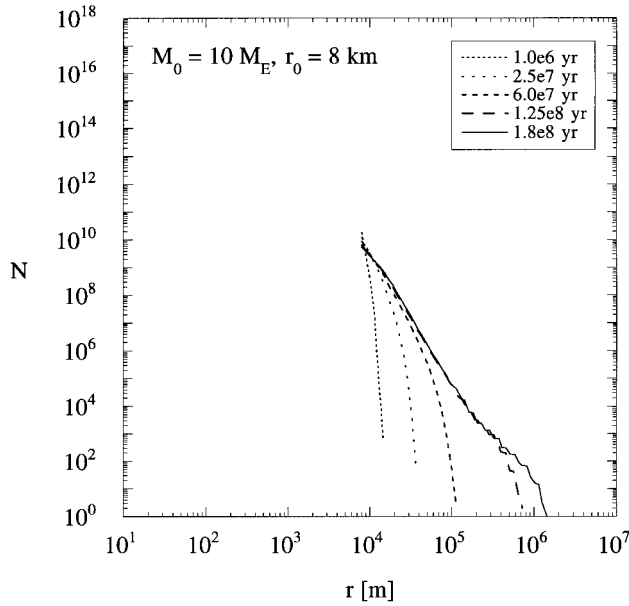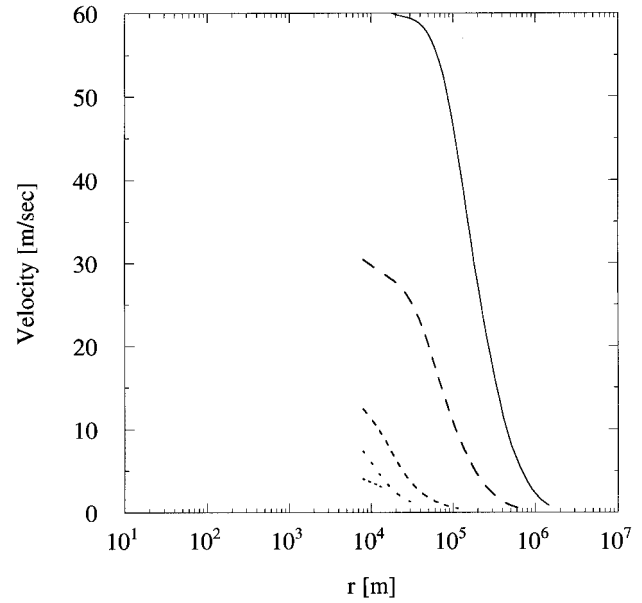
FIG. 8a

FIG. 8b

FIG. 8.—Model with $M_0 = 10M_E$, $r_0 = 8$ km, and $e = 10^{-3}$, with velocity evolution: (a) cumulative size distribution and (b) horizontal velocity as a function of time. Collisional growth is quasi-linear until the largest bodies have $r_{max} = 50$–100 km at 50–60 Myr. Runaway growth begins when $r_{max} \gtrsim 500$ km at ~ 100 Myr; these bodies then grow to sizes of 10^3 km in another 50–80 Myr.

somewhat larger particle velocities at the onset of runaway growth favor the growth of 50–100 km objects. The r_5 for these mass distributions is at least a factor of 2 larger than the r_5 for low e_{init} ($r_5 \approx 12$–15 km for $e_{init} = 10^{-2}$ compared with $r_5 \approx 6$–8 km for $e_{init} = 10^{-3}$). Models with larger r_0 are less successful. For $r_0 = 800$ m, runaway growth begins well after 100 Myr unless $M_0 \gtrsim (20$–$30)M_E$. Runaway growth always occurs on a very long timescale, $\gtrsim 150$–200 Myr, for $r_0 = 8$ km and $M_0 \lesssim 30M_E$.

Unlike the constant-velocity models, simulations with velocity evolution begin to develop a "runaway plateau" in the cumulative mass distribution when $r_{max} \gtrsim 500$ km (see Figs. 8–10). In constant-velocity simulations, we found two power-law cumulative mass distributions, $N_C \propto r^{-2.75}$ at low masses and $N_C \propto r^{-1.75}$ at large masses. The total mass per mass batch is then roughly constant at low masses and increases slowly with mass at large masses. In models *with* velocity evolution, dynamical friction reduces the velocities of the largest bodies to $V_i \lesssim 0.1$ m s^{-1} and maintains velocities of $V_i \sim 1$–10 m s^{-1} for smaller objects with $r_i \lesssim 10$ km. As noted by WS93, the increase in the escape velocity with mass coupled with the decrease in V_i produces substantial
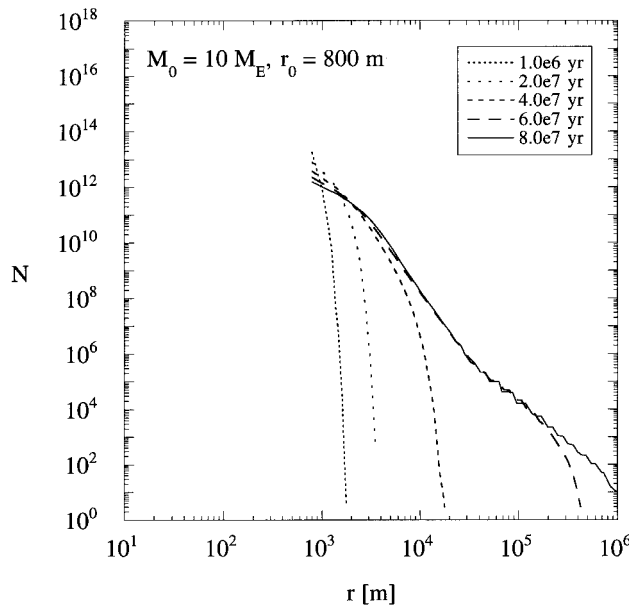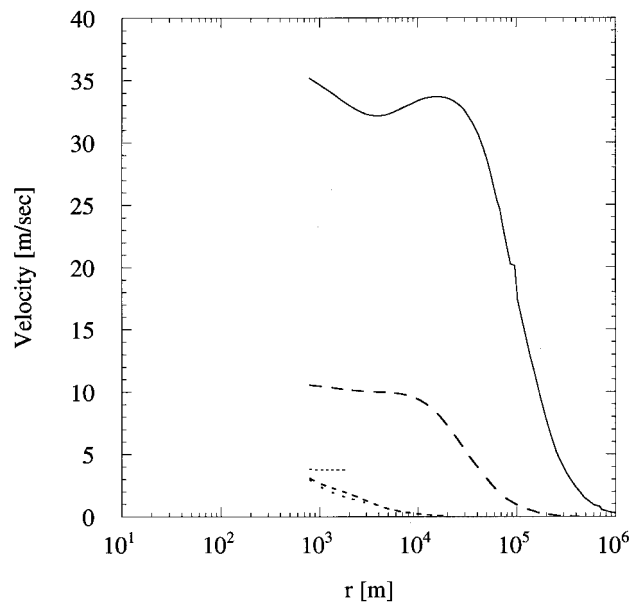

FIG. 9a

FIG. 9b

FIG. 9.—Same as Fig. 8, but for $r_0 = 800$ m. Collisional growth is quasi-linear for 45–50 Myr until the largest bodies have $r_{max} = 50$–100 km. The transition to runaway growth requires ~ 10 Myr, when Charon-sized objects form. These bodies grow to sizes of 1000 km in another 20 Myr. The velocities of the smallest objects increase with time as a result of viscous stirring. Dynamical friction reduces the velocities of the largest objects. The velocity minimum at 3–5 km indicates the batches that contain the largest fraction of the total mass.
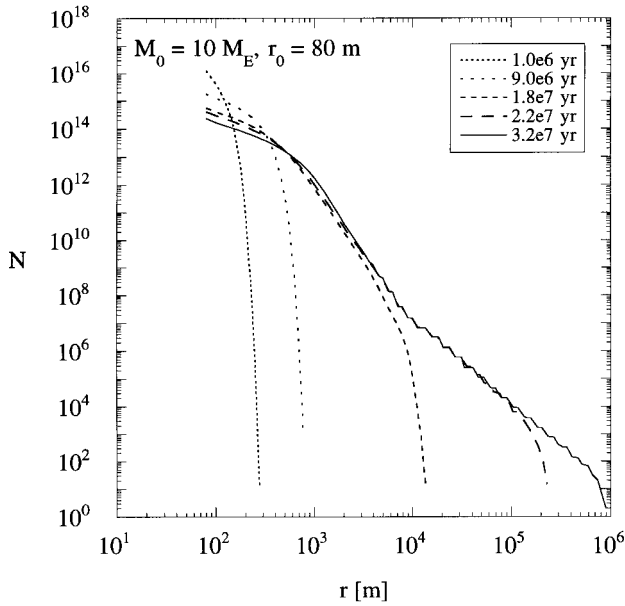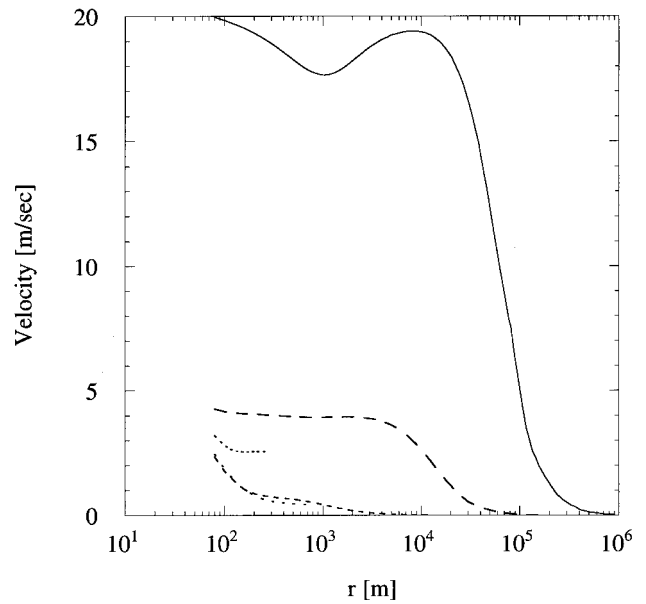
FIG. 10a

FIG. 10b

FIG. 10.—Same as Fig. 8, but for $r_0 = 80$ m. The largest bodies reach $r_{max} = 50$–100 km in 20 Myr and $r_{max} = 500$ km in only 25 Myr. Runaway growth begins at 25 Myr, and the largest bodies achieve $r_{max} \sim 1000$ km after another 8 Myr. As in Fig. 9, dynamical friction and viscous stirring increase the velocities of the smallest objects at the expense of the largest objects. Dynamical friction produces a velocity minimum in batches that contain the largest fraction of the total mass.

increases in the collisional cross sections (see also Wetherill & Stewart 1989; Barge & Pellat 1990, 1991, 1993; Ida & Makino 1992a, 1992b; Ohtsuki 1992; Kokubo & Ida 1996). In our models, the velocity distribution resembles a step function and produces a steplike increase in the gravitational focusing factors, from $F_g \sim 10$–100 at $r_i \sim$ 10–100 km up to $F_g \sim 10^4$ at $r_i \sim 300$–1000 km. Runaway growth then converts the $N_C \propto r^{-1.75}$ mass distribution into $N_C \approx$ const, because objects with $r_i \sim 100$–200 km grow too slowly to fill in the power law as objects with $r_i \gtrsim 500$ km run away. At low masses, the size distribution

remains a power law, $N_C \propto r^{-2.75}$, because runaway growth does not change the size distribution significantly.

To conclude this section, Figure 13 summarizes results for accretional evolution in the Kuiper Belt with velocity evolution and no fragmentation. Successful simulations that produce $\sim 10^5$ KBOs and a few Pluto-sized objects on time-scales of 100 Myr or less have initial masses somewhat larger than that predicted for a minimum-mass solar nebula extrapolated into the Kuiper Belt, $M_0 \gtrsim 10 M_E$, and bodies with initial radii of $r_0 \approx 800$ m to 8 km. Simulations with smaller initial bodies, $r_0 \sim 80$ m, produce Pluto-sized
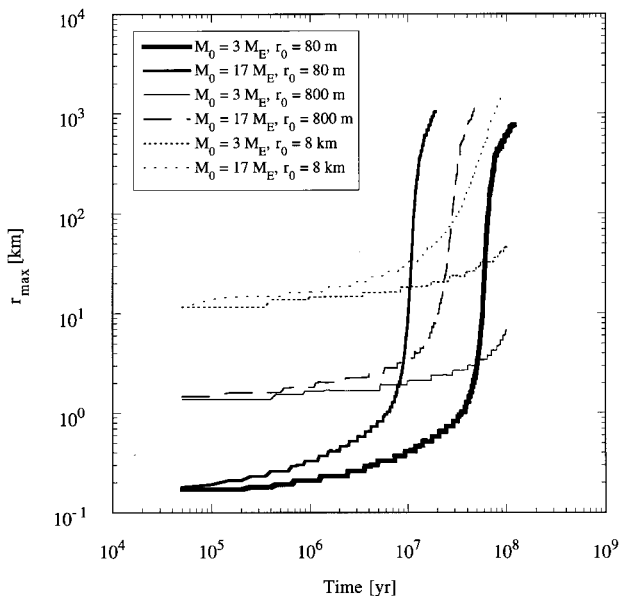

FIG. 11.—Evolution of the maximum radius with time for models with different initial mass (M_0) and initial radius (r_0), for low initial eccentricity $(e = 10^{-3})$. The timescale to reach runaway growth decreases with smaller r_0 and with larger M_0.
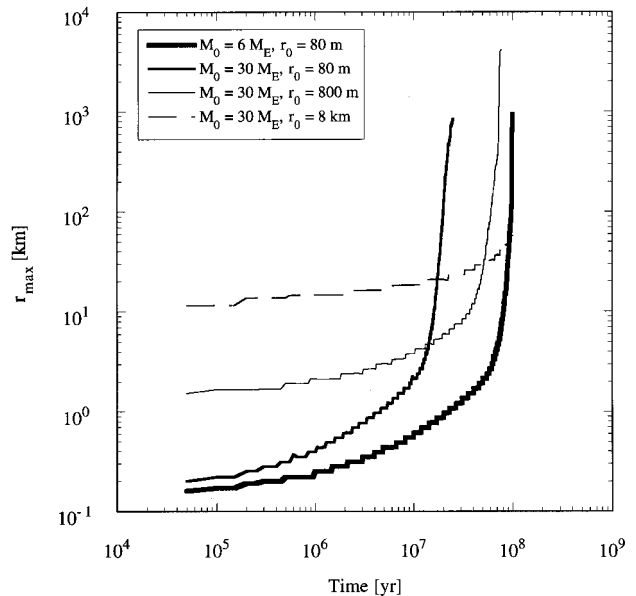

FIG. 12.—Evolution of the maximum radius as in Fig. 11, for models with large initial eccentricity $(e = 10^{-2})$. Models with high e require 2–4 times more mass to reach runaway growth on timescales similar to that of low-e models.
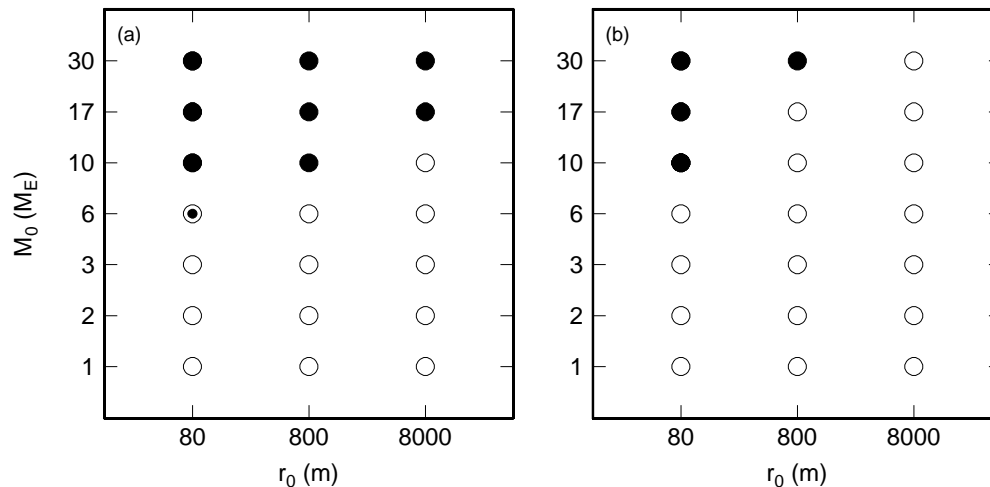
FIG. 13.—Summary of velocity evolution models for (a) $e = 10^{-3}$ and (b) $e = 10^{-2}$. Filled circles indicate successful simulations that produce a few Pluto-sized objects and $\sim 10^5$ KBOs in ≤ 100 Myr; open circles indicate simulations that produce no "Plutos" and too few KBOs in ≤ 100 Myr; filled circles within a larger open circle indicate partially successful simulations that produce a few Pluto-sized objects but too few KBOs in ≤ 100 Myr.

objects but too few KBOs in 100 Myr. In these partially successful models, runaway growth removes KBOs from the mass distribution more rapidly than they are produced from lower mass objects. This evolution does not occur in models with larger initial bodies, because collisional damping is less effective at "circularizing" the orbits during the orderly growth phase. The higher particle velocities in these models allow formation of more KBOs during the runaway growth of Charon-sized objects.

Collisional evolution often fails to produce 100+ km objects on any useful timescale. Simulations with $M_0 \approx (1-6)M_E$ produce neither Pluto-sized objects nor a substantial number of 100+ km KBOs in 100 Myr. Large initial eccentricities exacerbate this problem for models with $r_0 \gtrsim 800$ m, because collisional damping cannot reduce the particle velocities before 100+ km objects form. These simulations can produce KBOs and "Plutos" on longer timescales, 100–1000 Myr, in systems where a Neptune-sized object does not constrain the formation time. Extrapolating our results to smaller initial masses, simulations with $M_0 \lesssim 0.1 M_E$ fail to produce KBOs during the age of the solar system, ~ 5 Gyr.

3.4. *Limitations of the Models*

Statistical simulations of planetesimal growth have well-documented approximations and uncertainties. The model assumes a homogeneous spatial distribution of planetesimals whose velocities are small compared with the orbital velocity. These assumptions are good during the early stages of planetesimal evolution. As planetesimals grow, dynamical friction can reduce the velocities of high-mass objects below limits where the statistical approach is valid (Barge & Pellat 1990). Once this limit is reached, runaway growth produces a few large bodies that are not distributed homogeneously in space (WS93; Kokubo & Ida 1996). These large bodies can then pump up the velocities of the smallest bodies on short timescales through viscous stirring (Fig. 7). We end the simulations with velocity evolution during the runaway growth stage when the basic assumption of a homogeneous distribution of planetesimals begins to break down. The velocities of low-mass bodies remain small compared with the Keplerian velocity, but the most

massive objects often have velocities below the low-velocity limit of the kinetic approximation. We will discuss this problem below.

The remaining limitations of the statistical approach involve our implementation of standard algorithms. We adopt a single accumulation zone and thus cannot follow the evolution in semimajor axis of a planetesimal swarm (see Spaute et al. 1991). We use a coarser grid than some simulations, but this choice has little impact on the results at 35 AU. At 1 AU, the lag of simulations with $\delta > 1.1$ relative to a simulation with $\delta = 1.1$ increases with increasing δ; we find a 12% lag for $\delta = 1.4$ but only a 2%–3% lag for $\delta = 1.25$. At 35 AU, the lag in runaway growth relative to a $\delta = 1.1$ model increases from 4%–5% for $\delta = 1.4$ to 10%–15% at $\delta = 2$. Our $\delta = 1.4$ simulations thus overestimate the runaway growth time only by 4%–5% (see also Wetherill 1990; Kolvoord & Greenberg 1992). This error is small compared with other uncertainties in the calculation.

Our choice of the initial mass distribution has a modest impact on our results. We calculated the evolution of several size distributions with equal mass per mass batch for $r_{min} \lesssim r_i \lesssim r_{max}$. Simulations with $r_{min} \sim 100$–1000 m and $r_{max} \lesssim$ a few km are nearly indistinguishable from simulations with a single starting radius, $r_0 \approx r_{max}$. In these models, collisional damping effectively reduces all particle velocities as described above and allows runaway growth to occur. Simulations with large $r_{max} \approx 8$ km are similar to those with a single starting mass, unless r_{min} is small. For $r_{min} \lesssim 800$ m, collisional damping keeps the particle velocities small compared with models with a single starting mass. Runaway growth occurs in these models, but the timescale to runaway is sensitive to r_{min}. We plan to explore this sensitivity in more detail when we include fragmentation in the calculation.

The most uncertain approximation in our calculations is the treatment of low-velocity collisions. During the late stages of most simulations, the massive bodies have very low velocities and very large gravitational ranges. The velocities are often smaller than the Hill velocity, V_H, which invalidates the basic assumptions for our velocity evolution calculations (Barge & Pellat 1990, 1991, 1993). Barge & Pellat (1990) and WS93 have developed different approx-

imations to low-velocity collisions based on Ida's (1990) *N*-body simulations (see also Ohtsuki 1992). We note that these two approximations produce different velocities for high-mass planetesimals, which we plan to examine in more detail when we include fragmentation in our calculations. The mass evolution of runaway bodies is not affected by our treatment of velocity evolution in the low-velocity regime.

The large gravitational ranges of the most massive bodies also invalidate the standard treatment of collisions. We use the WS93 prescription for isolating the largest bodies from collisions with one another and adopt the Greenberg et al. (1991) approach to low-velocity collisions in the two-dimensional regime. Removing the isolation criteria allows the largest body to grow more rapidly than the isolated bodies and reduces the timescale to runaway growth by 5%–10%. Removing the Greenberg et al. (1991) two-dimensional cross sections has no substantial effect on our results.

Aside from fragmentation, we have included all important physical processes in planetesimal evolution. Our neglect of fragmentation, however, is a serious limitation. In previous simulations, fragmentation of relatively strong bodies with $r_i \gtrsim 1$–10 km produces a significant amount of cratering debris that can be accumulated later by runaway bodies (e.g., WS93; Barge & Pellat 1993). This process usually becomes important only in the late stages of calculations at 1 AU: it slows growth during early stages but speeds up runaway growth later in the evolution (Barge & Pellat 1993; WS93). However, collisions between very weak bodies can disrupt and thereby prevent *any* growth of icy planetesimals at modest velocities. The importance of fragmentation at $a \approx 35$ AU thus depends on the unknown strength of KBOs.

We can estimate the importance of fragmentation in Kuiper Belt simulations using Barge & Pellat's (1993) results for a reasonable fragmentation model. They adopt the Housen, Schmidt, & Holsapple (1991) energy prescription for planetesimal disruption and derive collisional outcomes for several test cases. These results are most appropriate for rocky asteroids, but it is straightforward to scale them to the weaker, icy bodies that might exist at 35 AU. We consider the two cases recently adopted by Stern & Colwell (1997a, 1997b): strong, rocky KBOs and weak, icy KBOs.

Fragmentation does not significantly change our main conclusions if KBOs are strong objects. According to Figure 5 of Barge & Pellat (1993), fragmentation modifies the growth of 10 km bodies only when $e \gtrsim e_{crit} \approx 0.025$. The critical eccentricity for fragmentation decreases to $e_{crit} \approx 10^{-2}$ for 1 km objects and $e_{crit} \approx 2 \times 10^{-3}$ for 0.1 km objects (see also Fig. 1 of Stern 1996). Our low-*e* simulations never reach these critical values. Fragmentation is important in large-*e* simulations, but most of these models do not produce KBOs on a reasonable timescale.

The growth of icy KBOs is probably very sensitive to the timescale for velocity evolution. We expect fragmentation to dominate the early evolution of all simulations considered above, because only objects with $r_i \gtrsim 20$–30 km can survive collisions and produce larger bodies (see also Stern & Colwell 1997a, 1997b). As the evolution proceeds, however, inelastic collisions should damp the velocities of bodies with $r_i \lesssim 1$ km, while dynamical friction damps the velocities of the most massive objects (see Fig. 7). These damping timescales are short compared with the viscous

stirring timescales, so the particle velocities decrease on relatively short timescales, ~ 10 Myr. This damping is probably sufficient to allow the growth of 1–10 km objects on timescales similar to those found in our models without fragmentation. Smaller bodies may not grow unless dynamical friction is very efficient. We will explore this possibility in our second paper.

4. DISCUSSION AND SUMMARY

We have developed a time-dependent planetesimal evolution program similar to the WS93 code used to simulate the formation of terrestrial embryos from small bodies. The program incorporates coagulation with realistic cross sections and velocity evolution using the statistical formulation of Barge & Pellat (1990, 1991; see also Hornung et al. 1985). Our numerical solutions to the coagulation equation agree with analytic solutions for three standard test cases. Our results also agree with WS93's simulation of the formation of Earth at 1 AU. The present models do not incorporate fragmentation of bodies during collisions. We will include fragmentation in a separate paper.

We have considered two simple cases of planetesimal evolution in a 6 AU–wide annulus centered at 35 AU. Models without velocity evolution invariably produce several large bodies that accrete practically all of the material in the annulus. The runaway growth in these simulations occurs without dynamical friction or gas drag; it is a direct consequence of gravitational focusing. The time required to produce a runaway body in our models scales inversely with the initial mass of the annulus *and* with the initial radii and velocities of the planetesimals. For bodies with $r_0 = 80$–8000 m and $e_{init} = 10^{-3}$, our simulations produce runaway growth in 100 Myr for annular masses of roughly $(10$–$30)M_E$. The timescale for runaway growth increases to 700–2000 Myr for $e = 10^{-2}$. A minimum-mass solar nebula with $\Sigma \propto R^{-3/2}$ contains $(7$–$15)M_E$ in a 6 AU–wide annulus centered at 35 AU. These models thus reach runaway growth in a minimum-mass nebula on timescales comparable to the maximum formation timescale for Neptune (~ 50–100 Myr; Lissauer et al. 1995; Pollack et al. 1996). Runaway growth on much shorter timescales, ~ 10 Myr, requires annular masses that far exceed the minimum-mass solar nebula, $\sim 100M_E$ in a 6 AU–wide annulus for $e_{init} = 10^{-2}$ to 10^{-3}.

Models with velocity evolution produce runaway growth on a much wider range of timescales compared with constant-velocity calculations. First, dynamical friction and viscous stirring dominate the evolution of models with relatively large (8 km) initial bodies. The velocities of these bodies thus increase as collisions produce more massive objects. This velocity increase delays runaway growth by factors of 2 or more compared with constant velocity evolution. The delay in the runaway growth time increases with increasing e_{init}. In contrast, collisional damping dominates the evolution of models with smaller (80–800 m) initial bodies. These bodies "cool" until the largest objects have radii of 10–20 km. Dynamical friction and viscous stirring then "heat up" the small bodies, but this heating is small compared with the velocity increases of the $r_0 = 8$ km models. For $e_{init} = 10^{-3}$, collisional damping enhances collision rates and decreases the timescale to runaway growth by factors of 4–12 compared with constant-velocity calculations. Our simulations of minimum-mass solar nebulae with $e_{init} = 10^{-3}$ reach runaway growth on timescales of

20–40 Myr for 80 m initial bodies, 50–100 Myr for 800 m bodies, and 75–250 Myr for 8 km bodies. These timescales increase by factors of 2–4 for $e_{\rm init} = 10^{-2}$.

The formation of runaway bodies in constant-velocity simulations is surprising. Previous simulations demonstrated a need for dynamical friction, which decreases the velocities of the most massive objects (Wetherill & Stewart 1989, 1993; Barge & Pellat 1990, 1991; Ohtsuki 1992; Ida & Makino 1992a, 1992b; Kokubo & Ida 1996). Gravitational focusing then allows these bodies to sweep up lower mass bodies very rapidly. Kokubo & Ida (1996) summarize necessary and sufficient conditions for runaway growth and show that the ratio of the maximum mass of planetesimals to their mean mass increases dramatically during runaway growth. Our constant-velocity simulations satisfy the "necessary" condition for runaway growth,

$$2R_{{\rm H},ij}\Omega \lesssim V_{ij} \lesssim V_{e,ij} \,, \qquad (2)$$

but do not meet the "sufficient" condition,

$$\frac{dV}{dm} < 0 \,, \qquad (3)$$

because our velocities are constant with mass, $dV/dm = 0$. Nevertheless, the maximum mass, $M_{\rm max}$, of each constant-velocity simulation increases much more rapidly than the mean mass, $\langle m_i \rangle$ (Fig. 14). In Figure 14a, the ratio $M_{\rm max}/\langle m_i \rangle$ increases slowly during the orderly growth phase and then increases rapidly when several isolated bodies begin to accrete most of the mass in the annulus. This runaway growth is not as extreme as that seen in models with velocity evolution. We derive $M_{\rm max}/\langle m_i \rangle \approx 10^6$ in constant-velocity models, compared with $M_{\rm max}/\langle m_i \rangle \approx 10^8$–$10^{10}$ in models with velocity evolution (Fig. 14b). Dynamical friction is responsible for the larger increase in $M_{\rm max}/\langle m_i \rangle$ in models with velocity evolution.

Although the constant-velocity simulations are artificial, they are a useful guide to planetesimal growth in the outer solar system. Our results show that collisional damping by small bodies can overcome viscous stirring and keep particle velocities low at $a = 35$ AU. The relative efficiency of collisional damping should increase with a, because the collision rates decrease more rapidly with a than do the damping rates ($\tau_{\rm coll} \propto a^{-5/2}$ vs. $\tau_{\rm damp} \propto a^{-3/2}$). The situation in the outer solar system differs markedly from conditions at small a. In our simulations at 1 AU, bodies with $r_i \approx 80$–800 m grow to 10 km objects in ~ 1000 yr. As in the 35 AU simulations described above, collisional damping reduces the velocities of the small bodies by a factor of ~ 2 in 1000 yr. In contrast to our 35 AU models, viscous stirring and dynamical friction act quickly to increase velocities once larger bodies are produced at 1 AU. Aside from the longer timescale to reach runaway growth, this evolution then follows closely the simulations in Figures 1 and 2.

With these considerations in mind, we suggest a modest modification to the sufficient condition for runaway growth,

$$\frac{dV}{dm} \leq 0 \,, \qquad (4)$$

instead of the condition in equation (3). This condition maintains the relative growth rate necessary for runaway in a three-dimensional system,

$$\frac{1}{M}\frac{dm}{dt} \propto M^{1/3} \qquad (5)$$

(see Kokubo & Ida 1996), when the gravitational focusing factor is large (e.g., $V_{ij} \lesssim V_{e,ij}$).

In addition to this new criterion for runaway growth, our simulations show that Neptune and Pluto can grow in parallel at $a \approx 30$–35 AU. For a minimum-mass solar nebula, previous calculations indicate that Neptune reached its current size in no longer than 50–100 Myr (Ip 1989; Lissauer et al. 1995; Pollack et al. 1996). In our models of minimum-mass solar nebulae at 35 AU, 800 m objects grow to Pluto-sized planets on similar timescales. However,
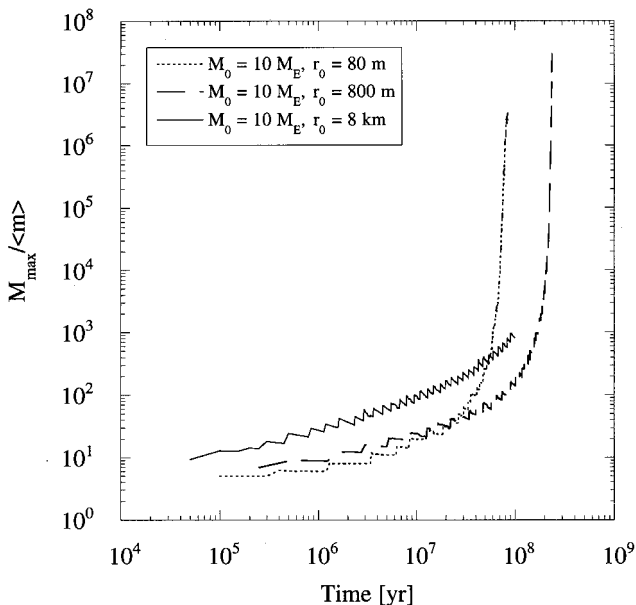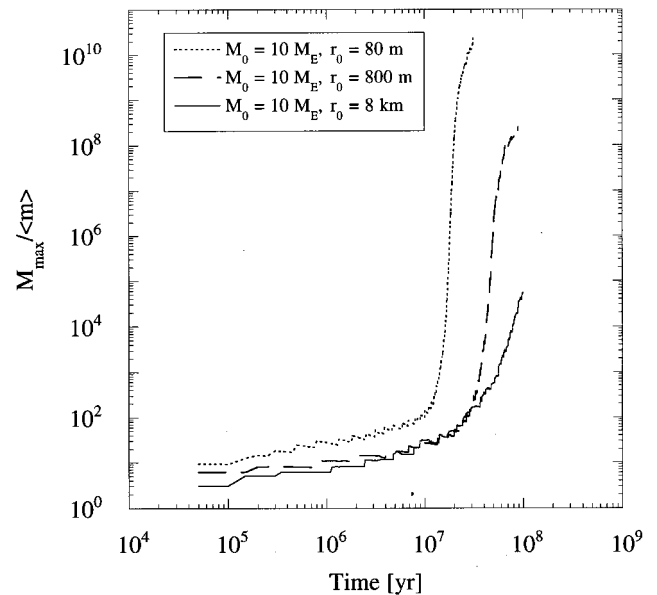

FIG. 14a

FIG. 14b

FIG. 14.—Evolution of $M_{\rm max}/\langle m \rangle$ as a function of time: (a) constant-velocity models; (b) with velocity evolution. The rapid increase in $M_{\rm max}/\langle m \rangle$ at the later stages of many simulations indicates runaway growth.

recent observations indicate a much shorter lifetime, ~ 5–10 Myr, for gaseous disks surrounding nearby pre–main-sequence stars (Sargent & Beckwith 1993; Strom et al. 1993; Russell et al. 1996; see also Fernández 1997). If our solar system evolved on a similar timescale, the formation of the gas-rich outer planets requires solar nebulae with masses 2–5 times larger than the minimum-mass solar nebula, M_{min} (Lissauer et al. 1995; Pollack et al. 1996). Neptune then attains its current size in 5–10 Myr. At 35 AU, objects reach 1000 km sizes in 10–20 Myr for $M_0 \approx (2$–$3)M_{min}$ and in 5–10 Myr for $M_0 \approx 5M_{min}$, assuming that the initial bodies have small masses and eccentricities. Fragmentation should not change these conclusions unless collisional erosion can prevent the formation of 1 km bodies from smaller building blocks.

Our Kuiper Belt simulation produce Pluto-sized objects on reasonable timescales for other plausible solar nebula models. In particular, Cameron's (1995 and references therein) detailed disk models for the protosolar nebula have a shallower density distribution, $\Sigma = \Sigma_0(a/a_0)^{-1}$, than the minimum-mass model we considered above to derive our success criteria (see also Ruden & Lin 1986; Ruden & Pollack 1991). Cameron's model contains $\sim 100M_E$ in our 6 AU annulus. The growth time for $1000+$ km objects scales simply from results with smaller disk masses. For models with velocity evolution, we estimate $\tau_r \approx 3$ Myr for $r_0 = 80$ m, $\tau_r \approx 8$ Myr for $r_0 = 800$ m, and $\tau_r \approx 15$ Myr for $r_0 = 8$ km. Although all of these models can produce Pluto-sized objects before Neptune reaches its final mass, models with $r_0 = 8$ km produce more KBOs with $r_i \sim 100$–300 km, as outlined in § 3.3.

These results—together with recent dynamical calculations of Malhotra (1993, 1995, 1996)—suggest a self-consistent picture for the formation of Pluto-Charon in the outer solar system. In this picture, Pluto and Charon begin as ~ 1 km planetesimals at $a \sim 35$–40 AU and grow to their present sizes on a timescale of 10–100 Myr. Both objects are runaway bodies more massive than the bulk of the planetesimal mass distribution and have low velocities due to collisional damping and dynamical friction. At a somewhat smaller semimajor axis, $a \approx 25$–30 AU, Neptune accretes its current mass in 10–100 Myr and migrates radially outward through the protosolar disk during the late stages of giant planet formation (Malhotra 1993; Pollack et al. 1996; Fernández & Ip 1996; see also Ipatov 1989, 1991). During this outward migration, Neptune captures Pluto-Charon in the 3:2 resonance (Malhotra 1995). This capture should effectively end further growth of Pluto-Charon, because the orbital elements increase to $e \sim 0.2$ and $i \sim 10°$ on a short timescale, ~ 10 Myr, inside the resonance (Malhotra 1995). High-velocity collisions within the resonance should also hinder growth as in our large-e models. Neptune also captures other KBOs at $a \approx 35$–40 AU into the 3:2 and other resonances (Malhotra 1996; see also Jewitt et al. 1996). Further growth of these objects is also slowed because of rapidly increasing velocities (Malhotra 1995, 1996; Morbidelli, Thomas, & Moons 1995; Davis & Farinella 1997). As long as collisional erosion does not decrease significantly the radii of captured KBOs, this sequence of events accounts for the general aspects of the mass distribution and orbital elements of observed KBOs in a simple way.

This picture for the formation of Neptune, Pluto-Charon, and KBOs differs from those of Stern (1995, 1996) and Stern & Colwell (1997a, 1997b), who studied KBO evolution at 40–70 AU. Stern & Colwell concluded that the formation of Neptune and KBOs, including Pluto-Charon, requires ~ 100–1000 Myr because of the low collision rates at $a \approx 30$–50 AU. Stern & Colwell's (1997a; see also Stern 1995, 1996) timescale for KBO formation is a factor of 10–20 longer than our timescale. Their results also conflict with the more detailed gas dynamic calculations of Pollack et al. (1996). Although the exact origin of this discrepancy is unclear, we suspect mass spacing, collision rates, and (less probably) fragmentation may be responsible. Our mass spacing, $\delta = 1.4$, should produce more accurate estimates for the growth time than $\delta = 2$ (Stern & Colwell 1997a) or $\delta = 4$ (Stern 1996). We estimate 10%–20% delays in runaway growth for $\delta = 2$ and expect very long delays for $\delta = 4$. In addition, our collision rates include a factor, β_{coll}, that accounts for the Gaussian distribution of impact velocities (Greenzweig & Lissauer 1992; see eq. [A12]). Neglecting this factor delays runaway growth by a factor of 3 (see also WS93). Stern (1995) does not include this factor in his cross section (see his eq. [5]) and thus derives much longer growth times. As noted above, our neglect of fragmentation encourages runaway growth. We do not think that including this process should delay runaway growth by another factor of 3, for reasons outlined earlier, and we plan to test this suspicion in our next paper.

However the theoretical issues may be resolved, several consequences of our accretion models can be tested with additional observations. All models that reach runaway growth produce 10–100 Pluto-sized objects with radii $r_{max} \approx 1000$–2000 km and a roughly power-law mass distribution with a maximum radius at $\sim (0.1$–$0.2)r_{max}$ (see Figs. 8–10). If Pluto and Charon are runaway bodies produced at $a \approx 35$–40 AU, there should be several additional "Plutos" with similar orbital elements. Malhotra (1995) reached a similar conclusion and noted that recent searches have not excluded the possibility of several additional such bodies in 3:2 orbital resonance with Neptune. The accretion models also predict a cumulative power-law distribution, $N_C \propto r^{-3}$, for objects with $r \lesssim 100$–200 km. By analogy with WS93, this shape is fairly independent of fragmentation as long as collisions produce overall growth instead of disruption. The best fit to the observed distribution is shallower than expected, $N_C \propto r^{-2}$, but the data are not yet accurate enough to preclude our model prediction (Jewitt et al. 1996). Larger surveys will provide a better test of this prediction (Luu et al. 1997).

Finally, our results suggest that KBO formation is likely in other solar systems. KBOs can grow in the dusty disks that surround many nearby main-sequence stars, if the disk masses are within an order of magnitude of the "maximum" disk masses for α Lyr, α PsA, and β Pic (Backman & Paresce 1993). Stars with disk masses near the minimum dust masses of these well-studied A-type stars probably have few, if any, KBOs but could have many objects with $r_i \sim 1$–10 km. Observations of nearby pre–main-sequence stars also indicate substantial masses, $M_d \gtrsim 10^3 M_E$, in circumstellar disks with radii of 100–1000 AU (e.g., Sargent & Beckwith 1993; see also Beckwith & Sargent 1996). These data imply $M_0 \sim (10$–$100)M_E$ in the Kuiper Belt. With formation timescales of 1–10 Myr, KBOs can grow in massive circumstellar disks during the pre–main-sequence contraction phase of a low-mass star (see Kenyon & Hartmann 1995 and references therein). In a less

massive disk, KBOs grow while the central star is on the main sequence. We expect no KBO formation in circumstellar disks with very low masses, $M_d \lesssim 10 M_E$. These disks can produce 1–10 km objects at $a \gtrsim 30$ AU, unless fragmentation prevents growth of icy bodies. We will explore this possibility in a subsequent paper.

APPENDIX

A1. OVERVIEW

Our evolution model follows procedures developed for other planetary formation calculations, including Safronov (1969), Greenberg et al. (1978, 1984), and WS93. We assume planetesimals are a statistical ensemble of masses with a distribution of horizontal and vertical velocities about a single Keplerian orbit. We consider a cylindrical annulus of width Δa and height H, centered at a radius a from the Sun. Particles in the annulus have a horizontal velocity $h_i(t)$ and vertical velocity $v_i(t)$ relative to an orbit with mean Keplerian velocity V_K (see Lissauer & Stewart 1993). These velocities are related to the eccentricity, e_i, and inclination, i_i, through

$$V_i^2 = (\tfrac{5}{8}e_i^2 + \tfrac{1}{2}\sin^2 i_i)V_K^2 , \tag{A1}$$

with

$$h_i^2 = \tfrac{5}{8}e_i^2 V_K^2 , \qquad v_i^2 = \tfrac{1}{2}\sin^2 i_i V_K^2 . \tag{A2}$$

We approximate the continuous distribution of particle masses with discrete batches having an integral number of particles, $n_i(t)$, and total masses $M_i(t)$ (WS93). The average mass of a batch, $m_i(t) = M_i(t)/n_i(t)$, evolves with time as collisions add and remove bodies from the batch. This procedure naturally conserves mass and allows a coarser grid than simulations with fixed mass bins (Wetherill 1990; see also Ohtsuki & Nakagawa 1988; Kolvoord & Greenberg 1992).

To follow the evolution of particle number, we solve the coagulation equations for all mass bins, k, during a time step, δt:

$$\delta n_k = \delta t(\epsilon_{ij} A_{ij} n_i n_j - n_k A_{ik} n_i) - \delta n_{k,\text{gd}} , \tag{A3}$$

$$\delta M_k = \delta t(\epsilon_{ij} A_{ij} n_i n_j m_k - n_k A_{ik} n_i m_k) - m_k \delta n_{k,\text{gd}} , \tag{A4}$$

where A_{ij} is the cross section, $\epsilon_{ij} = \tfrac{1}{2}$ for $i = j$ and $\epsilon_{ij} = 1$ for $i \neq j$. The three terms in equations (A3)–(A4) represent (1) mergers of m_i and m_j into a body of mass $m_k = m_i + m_j$, (2) loss of m_k through mergers with other bodies, and (3) loss of m_k by gas drag. This treatment assumes (1) that each body can collide with every other body and (2) that bodies do not fragment during collisions. Assumption 1 is correct for all but the very largest bodies, which become isolated from one another as their orbits circularize because of dynamical friction (see below). We correct equations (A3)–(A4) for this effect by calculating the "gravitational range" of the largest bodies—$R_{g,i} = K_1 a R_{H,ii_\text{mid}} + 2ae_i$ (WS93)—where $K_1 = 2(3)^{1/2}$ and $R_{H,ij} = [(m_i + m_j)/(3 M_\odot)]^{1/3}$ is the mutual Hill radius. As in WS93, the isolated bodies are the N largest bodies that satisfy the summation $\sum_{i_\text{min}}^{i_\text{max}} n_i R_{g,i} \geq \Delta a$. Assumption 2 is rarely correct, because all collisions produce some debris unless the relative velocity of the two particles is very low (see, e.g., WS93). In this paper, we concentrate on planetesimal growth and assume that all collisions result in mergers. We will consider the effects of fragmentation in a separate paper.

To calculate the appropriate index k for a specific collision between batches i and j, we first calculate a fixed grid of masses, m_l, for $l = 1$ to N_max and $\delta = m_{l+1}/m_l$. The mass spacing, δ, is constant throughout a calculation; N_max increases with time as more batches fill with particles. When a collision produces n_k bodies with m_k, we augment either batch l when $m_k \leq (m_l m_{l+1})^{1/2}$ or batch $l + 1$ when $m_k > (m_l m_{l+1})^{1/2}$. A complete cycle through all mass batches produces new values for n_k and M_k, which yield new values for the average mass per bin, $m_k = M_k/n_k$. This process conserves mass and provides a good description of coagulation when δ is small (see below).

Besides collisions, several processes contribute to the velocity evolution of growing planetesimals, including dynamical friction, gas drag, and viscous stirring. We assume that all collisions between mass batches conserve the horizontal and vertical components of kinetic energy, $E_{h,i} = \tfrac{1}{2}m_i h_i^2$ and $E_{v,i} = \tfrac{1}{2}m_i v_i^2$. The change in the two components of kinetic energy due to collisions is

$$\delta E_{h,k}^{\text{co}} = -\tfrac{1}{2}[\delta(m_k h_k^2) = \delta n_i(m_i h_i^2) + \delta n_j(m_j h_j^2)] , \tag{A5}$$

$$\delta E_{v,k}^{\text{co}} = -\tfrac{1}{2}[\delta(m_k v_k^2) = \delta n_i(m_i v_i^2) + \delta n_j(m_j v_j^2)] \tag{A6}$$

for each pair of collisions between m_i and m_j. In these expressions, $\delta n_i \leq 0$ represents the change in n_i due to collisions with particles in batch j. Batch k loses kinetic energy because of collisions with other batches (i.e., $\delta n_k > 0$). We also calculate the evolution of h_i and v_i due to gas drag (Adachi, Hayashi, & Nakazawa 1976) and collective interactions, such as dynamical friction and viscous stirring, using a statistical treatment of the appropriate Boltzmann and Fokker-Planck equations

(Hornung et al. 1985; see § A3 below). The complete change in the horizontal and vertical kinetic energies is thus

$$\delta E_{h,k} = \delta E_{h,k}^{\rm co} + \delta E_{h,k}^{\rm gd} + \delta E_{h,k}^{\rm in} + \delta E_{h,k}^{\rm lr} , \tag{A7}$$

$$\delta E_{v,k} = \delta E_{v,k}^{\rm co} + \delta E_{v,k}^{\rm gd} + \delta E_{v,k}^{\rm in} + \delta E_{v,k}^{\rm lr} , \tag{A8}$$

where the superscripts "gd" (gas drag), "in" (inelastic), and "lr" (long-range elastic collisions, such as viscous stirring and dynamical friction) refer to a specific type of velocity evolution outlined below (see also Barge & Pellat 1990, 1991; WS93).

We solve the complete set of evolution equations (eqs. [A3], [A4], [A7], and [A8]) using an explicit method that automatically prevents large changes ($>0.1\%$) in the dynamical variables—n_i, M_i, h_i, and v_i—by limiting the time step. As in WS93, we require integer values for n_i and δn_i. Section A4 compares our numerical procedures with analytic results from Wetherill (1990; see also Ohtsuki & Nakagawa 1988; Ohtsuki, Nakagawa, & Nakazawa 1990). Section 2 of the main text compares calculations at 1 AU with results from WS93. In both cases, our procedures reproduce the expected results. Before describing the analytic results, we first describe in detail our treatment of the collision rates (§ A2) and the velocity evolution (§ A3).

A2. COLLISION RATE

Approximations to the collision rates between planetesimals are in the spirit of kinetic theory, where the number of collisions is the product of the local density, the relative velocity, and a cross section. WS93 express the number of collisions between a single body, m_i, and all of the bodies, m_j, as

$$n_{c,ij} = \alpha_{\rm coll}\left(\frac{n_j}{4Ha\,\Delta a}\right)V_{ij}F_{g,ij}(r_i + r_j)^2\delta t , \tag{A9}$$

where r_i and r_j are the radii of the two bodies, $V_{ij}^2 = V_i^2 + V_j^2$ is the relative velocity, and $F_{g,ij}$ is the gravitational focusing factor. The constant factor $\alpha_{\rm coll}$ accounts for the Gaussian distribution of particle velocities and the difference between the collisional frequencies of particles on Keplerian orbits and those in a box (Greenzweig & Lissauer 1992; WS93). The relative velocities and scale height depend on the individual particle velocities:

$$H = \sqrt{2}\Omega^{-1}(v_i^2 + v_j^2)^{1/2} , \qquad V_{ij} = (h_i^2 + v_i^2 + h_j^2 + v_j^2)^{1/2} \tag{A10}$$

(WS93), where Ω is the Keplerian angular frequency. The total number of collisions for m_i is simply $n_i n_c$; the cross section appropriate for equations (A3)–(A4) is then

$$A_{ij} = \alpha_{\rm coll}\left(\frac{1}{4Ha\,\Delta a}\right)V_{ij}F_{g,ij}(r_i + r_j)^2 . \tag{A11}$$

We consider two approaches to compute the gravitational focusing factor, $F_{g,ij}$. In the first case, we follow WS93 and set

$$F_{g,ij} = F_{{\rm WS},ij} = E_{ij}\left(1 + \beta_{\rm coll}\frac{V_{e,ij}^2}{V_{ij}^2}\right), \tag{A12}$$

where $V_{e,ij}^2 = 2G(m_i + m_j)/(r_i + r_j)$ is the mutual escape velocity. The extra factors account for the Gaussian distribution of impact velocities ($\beta_{\rm coll}$; Greenzweig & Lissauer 1992) and the deviations from two-body focusing at low relative velocities (E_{ij}; Greenzweig & Lissauer 1990). We adopt WS93's prescription for the variation of $\beta_{\rm coll}$ as a function of the relative velocity in Hill units, $V_{{\rm H},ij} = V_{ij}/(R_{{\rm H},ij}V_{\rm K}/a)$:

$$\beta_{\rm coll} = \begin{cases} 2.7 , & \text{if } V_{{\rm H},ij} > 2 , \\ 1.0 + 1.7(V_{{\rm H},ij} - 1) , & \text{if } 1 \le V_{{\rm H},ij} \le 2 , \\ 1.0 , & \text{if } V_{{\rm H},ij} < 1 , \end{cases} \tag{A13}$$

and we set

$$E_{ij} = \begin{cases} 1 , & \text{if } V_{ij} > 0.13 V_{e,ij} , \\ \dfrac{4(e^2 + \sin^2 i)^{1/2}E_k}{\pi^2 \sin i} , & \text{if } V_{ij} \le 0.13 V_{e,ij} , \end{cases} \tag{A14}$$

where $E_k = \int_0^{\pi/2}(1 - k^2 \sin^2 \theta)^{1/2}d\theta$ for $k^2 = 3/(4[1 + (\sin i)/e])$ (Greenzweig & Lissauer 1990; Greenberg et al. 1991).

At very low velocities ($V_{{\rm H},ij} < 2.3$), we adopt the two-body collisional cross sections of Greenberg et al. (1991):

$$F_{{\rm 2B},ij} = \begin{cases} \left(1 + \dfrac{V_{e,ij}^2}{V_{\rm T}^2}\right)\dfrac{V_{\rm T}}{V_{ij}}\dfrac{R_{\rm H}}{R_{\rm T}} , & \text{if } V_{{\rm H},ij} < 2.3 , \\ 0.5\left(1 + \dfrac{V_{e,ij}^2}{V_{\rm T}^2}\right)^{1/2}\dfrac{V_{\rm T}}{V_{ij}}\dfrac{R_{\rm H}}{R_{\rm T}}\dfrac{H}{r_i + r_j} , & \text{if } V_{{\rm H},ij} < 2.3, \ v_{{\rm H},ij} < v_{{\rm H,crit}} , \end{cases} \tag{A15}$$

where $R_{\rm T} = a[(m_i + m_j)/(1\ M_\odot)]^{2/5}$ is the Tisserand radius, $V_{\rm T} = 1.1\Omega\Delta a_{\rm T}$ is the Tisserand velocity, $\Delta a_{\rm T} = 2.5 R_{\rm H}$ is the half-width of the feeding zone, $v_{{\rm H},ij} = v_{ij}/V_{\rm H}$ is the relative vertical velocity in Hill units, and $v_{\rm H,crit} < 0.7 \sin (0.9[(r_i + r_j)/R_{{\rm H},ij}]^{1/2})$.

In our second approach to gravitational focusing, we modify the piecewise analytic approximation of Spaute et al. (1991):

$$F_{\mathrm{S},ij} = \begin{cases} 1 + \beta_{\mathrm{coll}}(V_{e,ij}/V_{ij})^2\,, & \text{if } V_{ij} > 0.032 V_{e,ij}\,, \\ 42.4042(V_{e,ij}/V_{ij})^{1.2}\,, & \text{if } 0.01 < V_{ij}/V_{e,ij} \leq 0.032\,, \\ 10706.916\,, & \text{if } V_{ij}/V_{e,ij} \leq 0.01\,, \end{cases} \qquad (A16)$$

with β_{coll} as defined above. These expressions are continuous and serve as a check on the more detailed expressions for $F_{\mathrm{WS},ij}$. For very low velocity encounters, we use the two-body cross sections for $F_{2\mathrm{B}}$ defined above.

In these approximations to the cross section, the transition from F_{WS} or F_{S} to $F_{2\mathrm{B}}$ at $V_{\mathrm{H},ij} \approx 2.3$ is not smooth. To effect a smooth transition, we set

$$F_{g,ij} = \begin{cases} (1 - x_{2\mathrm{B},ij})F_{\mathrm{WS},ij} + x_{2\mathrm{B},ij} F_{2\mathrm{B},ij}\,, \\ (1 - x_{2\mathrm{B},ij})F_{\mathrm{S},ij} + x_{2\mathrm{B},ij} F_{2\mathrm{B},ij}\,, \end{cases} \qquad (A17)$$

where

$$x_{2\mathrm{B},ij} = \begin{cases} 0\,, & \text{if } V_{\mathrm{H},ij} > 3.3\,, \\ 0.5(V_{\mathrm{H},ij} - 2.3)\,, & \text{if } 1.3 < V_{\mathrm{H},ij} < 3.3\,, \\ 1\,, & \text{if } V_{\mathrm{H},ij} < 1.3\,. \end{cases} \qquad (A18)$$

A3. VELOCITY EVOLUTION

As noted above, kinetic models approximate planetesimal orbital elements as a mean square random velocity, V_i^2 (Safronov 1969; Stewart & Wetherill 1988; WS93 and references therein). We divide this velocity into horizontal, h_i, and vertical, v_i, components that are related to V_i, e, and i (see eqs. [A1]–[A2]). Hornung et al. (1985) have derived analytic expressions for the time evolution of planetesimal velocities using a kinetic approximation to average over the velocity distribution function. WS93 reformulated some of these results in terms of the eccentricity and inclination, and we adopt their expressions here for simplicity (see also Stewart & Wetherill 1988). We calculate velocity changes due to (1) gas drag, which decreases particle velocities and causes particles to spiral in through the disk; (2) dynamical friction from elastic collisions, which transfers kinetic energy from larger to smaller bodies; (3) viscous stirring from elastic collisions, which taps the solar gravitational field to increase the velocities of all bodies; and (4) collisional damping from inelastic collisions (see also Hornung et al. 1985; Barge & Pellat 1990, 1991; Ohtsuki 1992).

The time evolution of the eccentricity and inclination for long-range, elastic encounters is

$$\frac{de_{\mathrm{vs},i}^2}{dt} = \sum_{j=1}^{N} \frac{C_{\mathrm{lr}}}{4}(m_i + m_j)e_i^2(J_r + 4J_\theta)\,, \qquad \frac{di_{\mathrm{vs},i}^2}{dt} = \sum_{j=1}^{N} \frac{C_{\mathrm{lr}}}{2\beta_{ij}^2}(m_i + m_j)i_i^2 J_z \qquad (A19)$$

for viscous stirring and

$$\frac{de_{\mathrm{df},i}^2}{dt} = \sum_{j=1}^{N} \frac{C_{\mathrm{lr}}}{2}(m_j e_j^2 - m_i e_i^2)(K_r + 4K_\theta)\,, \qquad \frac{di_{\mathrm{df},i}^2}{dt} = \sum_{j=1}^{N} \frac{C_{\mathrm{lr}}}{2\beta_{ij}^2}(m_j i_j^2 - m_i i_i^2)K_z \qquad (A20)$$

for dynamical friction (WS93, Appendix C). In these expressions, e_i, e_j, i_i, and i_j are the eccentricity and inclination of each body, $\beta_{ij}^2 = (i_i^2 + i_j^2)/(e_i^2 + e_j^2)$ is the ratio of inclination to eccentricity, and $C_{\mathrm{lr}} = 16G^2\rho_j(\ln \Lambda + 0.55)/V_{\mathrm{K}}^3(e_i^2 + e_j^2)^{3/2}$ is a function of the density of particles in batch j and the relative horizontal velocity of the mass batches (WS93). The functions J_r, J_θ, J_z, K_r, K_θ, and K_z are definite integrals that are functions only of β_{ij} (Hornung et al. 1985; Barge & Pellat 1990, 1991; WS93; Ohtsuki 1992 describes a similar approach to velocity evolution).

The time evolution of e and i due to collisional damping is

$$\frac{de_{\mathrm{in},i}^2}{dt} = \sum_{j=0}^{i} \frac{C_{\mathrm{in}}}{2}[m_j e_j^2 - m_i e_i^2 - (m_i + m_j)e_i^2](I_r + 4I_\theta)\,, \qquad (A21)$$

$$\frac{di_{\mathrm{in},i}^2}{dt} = \sum_{j=0}^{i} \frac{C_{\mathrm{in}}}{\beta_{ij}^2}[m_j i_j^2 - m_i i_i^2 - (m_i + m_j)i_i^2]I_z\,, \qquad (A22)$$

where $C_{\mathrm{in}} = \alpha_{\mathrm{coll}}\epsilon_{ij}\rho_j V_{ij} F_{g,ij}(r_i + r_j)^2$ and ρ_j is the mass density (Hornung et al. 1985; see also Ohtsuki 1992). We include terms from the collision rate, α_{coll}, ϵ_{ij}, and $F_{g,ij}$, for consistency. The integrals, $I_r(\beta_{ij})$, $I_\theta(\beta_{ij})$, and $I_z(\beta_{ij})$, are listed in the appendices to Hornung et al. (1985). We integrate these expressions numerically. The I_z integral often diverges; we set $I_z = I - (I_r + I_\theta)$ to avoid these divergences.

In addition to dynamical friction and viscous stirring, we also consider velocity evolution due to gas drag. Gas drag reduces the velocities of all mass batches and also removes material from each mass match. The inward drift of material is

$$\frac{\Delta a}{a} = 2(0.97e + 0.64i + \eta/V_{\mathrm{K}})\frac{\eta}{V_{\mathrm{K}}}\frac{\delta t}{\tau_0} \qquad (A23)$$

(Adachi et al. 1976), where η is the gas velocity relative to the local Keplerian velocity, V_K. We adopt $\eta = 60$ m s^{-1} for calculations at 1 AU (WS93) and $\eta = 30$ m s^{-1} for calculations at 35 AU (Adachi et al. 1976). The characteristic drift time is

$$\tau_0 = \frac{365}{C_D}\left(\frac{m_i}{10^{21}\text{ g}}\right)^{1/3}\left(\frac{1\text{ AU}}{a}\right)\left(\frac{10^{-9}\text{ g cm}^{-3}}{\rho_g}\right)T_K ,\qquad(A24)$$

where $C_D = 0.5$ is the drag coefficient, $\rho_g = 1.18 \times 10^{-9}[a/(1\text{ AU})]^{-11/4}$ is the gas density (Nakagawa, Hayashi, & Nakazawa 1983), and T_K is the orbital period (see Adachi et al. 1976; WS93). To simulate the disappearance of gas in the protosolar nebula, we decrease the gas density with time:

$$\rho_g(t) = \rho_{g,0}\exp\left(-t/\tau_g\right)\qquad(A25)$$

with $\rho_{g,0} = 1.18 \times 10^{-9}[a/(1\text{ AU})]^{-11/4}(M_0/M_{\min})$ g cm^{-3} (Ruden & Lin 1986; Ruden & Pollack 1991; WS93). The radial decrease of the gas density follows models for minimum-mass solar nebulae; the mass dependence allows the density to scale with the mass of the annulus.

The number of bodies lost from the calculation at each time step depends on their effectiveness at crossing Δa. We set the number of bodies lost from a batch as

$$\frac{\delta n_{\mathrm{gd},i}}{n_i} = \frac{\Delta a}{a}\frac{\delta t}{\tau_0} .\qquad(A26)$$

This expression is used in equations (A3)–(A4).

Finally, we adopt Wetherill & Stewart's (1989) expression for velocity damping due to gas drag:

$$\frac{dV_i}{dt} = \frac{-\pi C_D}{2m_i}\rho_g V_g^2 r_i^2 ,\qquad(A27)$$

where $C_D = 0.5$ is the drag coefficient and $V_g = [V_i(V_i + \eta)]^{1/2}$ is the mean relative velocity of the gas.

We convert the differential equations, (A19)–(A22) and (A27), into a kinetic energy form in two steps. We use β_i to derive the appropriate horizontal and vertical components of the velocity, V_i, in equation (A27). Equation (A2) similarly yields δh_i and δv_i in terms of δe_i and δi_i, where

$$\delta e_i^2 = \delta t\left(\frac{de^2}{dt}\right),\qquad \delta i_i^2 = \delta t\left(\frac{di^2}{dt}\right).\qquad(A28)$$

These substitutions yield

$$(\delta h_i^{\mathrm{gd}})^2 = -\delta t\left[\frac{\pi C_D \rho_g V_g^2 r_i^2}{2m_i(1 + 0.8\beta_i^2)}\right],\qquad (\delta v_i^{\mathrm{gd}})^2 = 0.8\beta_i^2\,\delta h_i^2 ,\qquad(A29)$$

$$(\delta h_i^{\mathrm{in}})^2 = \frac{5}{8}V_K^2\,\delta t\left(\frac{de_{\mathrm{in},i}^2}{dt}\right),\qquad (\delta v_i^{\mathrm{in}})^2 = \frac{1}{2}\sin^2 i V_K^2\,\delta t\left(\frac{di_{\mathrm{in},i}^2}{dt}\right),\qquad(A30)$$

$$(\delta h_i^{\mathrm{lr}})^2 = \frac{5}{8}V_K^2\,\delta t\left(\frac{de_{\mathrm{vs},i}^2}{dt} + \frac{de_{\mathrm{df},i}^2}{dt}\right),\qquad (\delta v_i^{\mathrm{lr}})^2 = \frac{1}{2}\sin^2 i V_K^2\,\delta t\left(\frac{di_{\mathrm{vs},i}^2}{dt} + \frac{di_{\mathrm{df},i}^2}{dt}\right).\qquad(A31)$$

We multiply these relations by m_i for substitution into equations (A7)–(A8).

A4. TESTS OF THE EVOLUTION CODE

To test the validity of our numerical techniques, we compare our results with several test cases (see Ohtsuki & Nakagawa 1988; Ohtsuki et al. 1990; Wetherill 1990). The coagulation equations (eqs. [A3]–[A4]) have analytic solutions for three simple forms of the cross section, A_{ij}. Von Smoluchowski (1916) first solved the coagulation equation for $A_{ij} = \alpha_c = $ const. Trubnikov (1971) described solutions for $A_{ij} = \beta_c(m_i + m_j)$ and $A_{ij} = \gamma_c m_i m_j$. Wetherill (1990) identified an inconsistency in Trubnikov's results for $A_{ij} = \gamma_c m_i m_j$ and showed that this cross section produces runaway growth. Tanaka & Nakazawa (1994) verified Wetherill's new solution and placed limits on the validity of the coagulation equation during runaway growth.

The analytic solutions to the coagulation equation provide rigorous tests of numerical methods. Two simple cases, $A_{ij} = \alpha_c$ and $A_{ij} = \beta_c(m_i + m_j)$, do not lead to runaway growth, but they test the ability of numerical codes to reach a target mass at a specified time. They also yield estimates for mass conservation over many time steps. Numerical solutions for $A_{ij} = \gamma_c m_i m_j$ are challenging, because runaway growth requires a careful, automatic procedure for changing the time step. In all three cases, the time lag between the analytic and numerical solutions depends on the mass ratio between consecutive batches, δ (Wetherill 1990). These tests thus yield a quantitative measure of the largest allowed value for δ (Ohtsuki & Nakagawa 1988; Ohtsuki et al. 1990; Wetherill 1990).

To compare our numerical results with analytic solutions, we follow conventions established by Ohtsuki et al. (1988) and Wetherill (1990). For $A_{ij} = \alpha_c$ and $A_{ij} = \beta_c(m_i + m_j)$, we plot $\log N_i m_i^2$ as a function of $\log m_i$. We evaluate $\log N_k$ as a function

of log m_k and the fractional mass in the small-body swarm and the runaway body as a function of a dimensionless time for $A_{ij} = \gamma_c m_i m_j$. The numerical calculations do not have regular mass intervals, so we calculate $N = \delta N/\delta m$, where

$$\delta N = N_k + \tfrac{1}{2}(N_{k+1} + N_{k-1}), \qquad \delta m = m_{k+1} - m_{k-1}. \tag{A32}$$

Wetherill (1990) describes analytic solutions for each cross section in detail. The $A_{ij} = \alpha_c$ case has the simplest solution. If n_0 is the initial number of particles with mass m_i, the number of bodies with mass $m_k = k m_i$ at a time t is

$$n_k = n_0 f^2 (1 - f)^{k-1}, \tag{A33}$$

where $f = 1/(1 + \tfrac{1}{2}\eta_1)$ and $\eta_1 = \alpha_c n_0 t$ is the dimensionless time (see also Silk & Takahashi 1979; Ohtsuki & Nakagawa 1988). The solution for $A_{ij} = \beta_c(m_i + m_j)$ has a similar form:

$$n_k = n_0 \frac{k^{k-1}}{k!} f(1 - f)^{k-1} \exp\left[-k(1 - f)\right], \tag{A34}$$

where $f = \exp(-\eta_2)$ and $\eta_2 = \beta_c n_0 t$. In both of these expressions, f is the fraction of bodies with m_i that have yet to undergo a collision at time t.

Models with $A_{ij} = \gamma_c m_i m_j$ lead to runaway growth when $\eta_3 = \gamma n_0 t = 1$ (Wetherill 1990; Barge & Pellat 1990; Tanaka & Nakazawa 1994). The number distribution for $\eta_3 \leq 1$ is

$$n_k = n_0 \frac{(2k)^{k-1}}{k!k} (\eta_3/2)^{k-1} \exp(-k\eta_3). \tag{A35}$$

This solution fails to conserve mass for $\eta_3 > 1$; a single runaway body then contains most of the total mass. The mass of the runaway body for $\eta_3 > 1$ is

$$m_R = n_0 \exp\left[-\int \sum_{k=1}^{N} k^2 (n_k/n_0) d\eta'\right] \tag{A36}$$

(Wetherill 1990; Tanaka & Nakazawa 1993, 1994).

Figure 15 compares our results for $\delta = 1.25$ with the analytic solution for $A_{ij} = \alpha_c$. The agreement is good and again improves as δ decreases. Our results for $\delta = 1.4$–1.6 are consistent with the analytic solution, although we have too few mass batches to make reliable comparisons when $\eta_1 < 10$–20. We did not attempt numerical models for $\delta = 1.6$–2 (the maximum allowed), but we expect that these will produce satisfactory results for $\eta > 100$.

Figure 16 shows results for $A_{ij} = \beta_c(m_i + m_j)$ and $\delta = 1.25$. The agreement between our calculation and the analytic solution is quite good and improves as δ increases. We find a slight excess of low-mass bodies in our numerical results compared with the analytic solution. Wetherill's Figure 4 contains a similar excess. The peak of our normalized number distribution lags the analytic result by 1.4%. This lag decreases with δ and is less than 1% for $\delta = 1.10$.
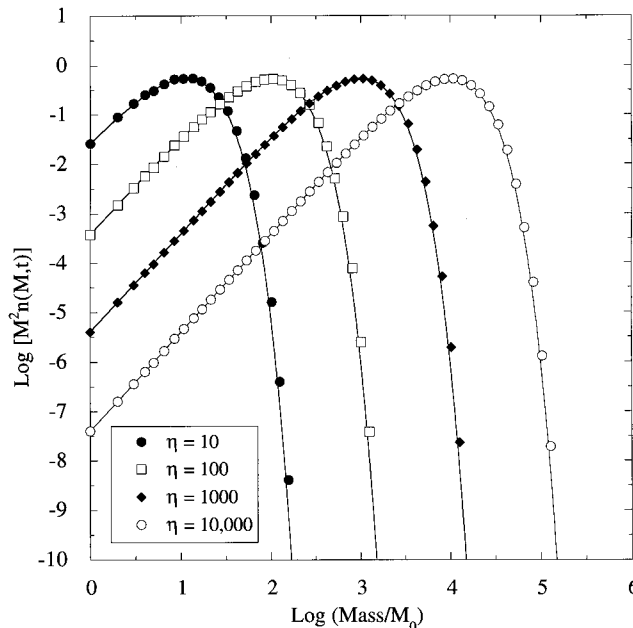

FIG. 15.—Evolution of the mass distribution for a constant cross section, $A_{ij} = \alpha_c$. The solid curves plot analytic results for four values of η; the symbols indicate results of the numerical simulations.
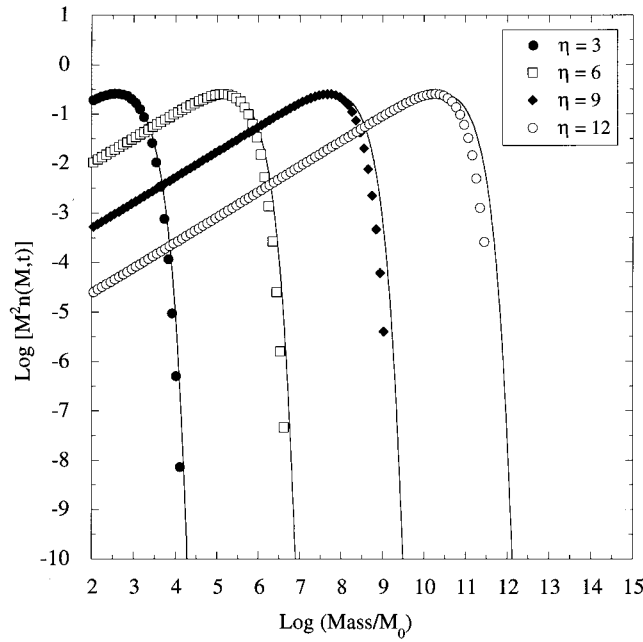
FIG. 16.—Same as Fig. 15, but for $A_{ij} = \beta_c(M_i + M_j)$

Figures 17 and 18 summarize our results for $A_{ij} = \gamma_c m_i m_j$ and $\delta = 1.25$ for $\eta \leq 1$. The numerical solution follows the analytic model very closely for $\eta_3 < 0.95$ and then begins to diverge at large masses as η approaches unity (Fig. 17). The numerical model begins runaway growth at $\eta_3 = 1.012$ and lags the analytic model by 1.2%. The numerical runaway begins much closer to the predicted result, $\eta_3 = 1.005$, for $\delta = 1.08$. Larger values for δ produce runaways that are delayed by much longer factors. The lag is 2.7% for $\delta = 1.4$ and 8.7% for $\delta = 2$. Wetherill (1990) quotes similar results for his numerical models with $\delta = 1.07$ and $\delta = 1.25$.

Figure 18 describes the evolution of the runaway-growth model for $\delta = 1.08$ and $\eta_3 > 1$. The calculated mass distribution initially lags the analytic result by less than 1% for η_3 marginally larger than 1 (see also WS93) but matches the analytic result almost exactly at $\eta_3 = 1.05$ (Fig. 18a). The calculation continues to match the analytic result until $\eta_3 \approx 5$. Figure 18b plots the mass of the runaway body for $\eta_3 \geq 1$. The calculated mass agrees with the analytic prediction, equation (A36), to 1% or better for all $\eta_3 \geq 1$. Models with $\delta = 1.25$ have greater difficulty reaching large η_3 as a result of their poorer mass resolution. These
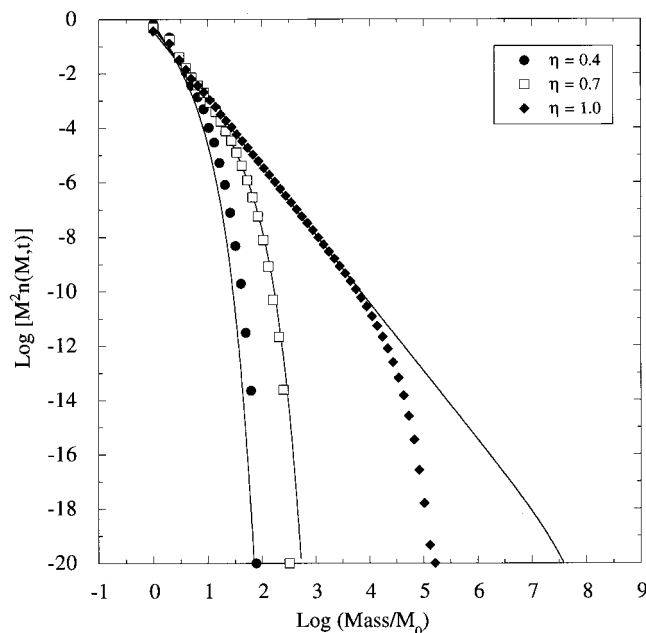

FIG. 17.—Evolution of the mass distribution for $A_{ij} = \gamma_c M_i M_j$. The solid curves plot analytic results for four values of η; the symbols indicate results of the numerical simulations.
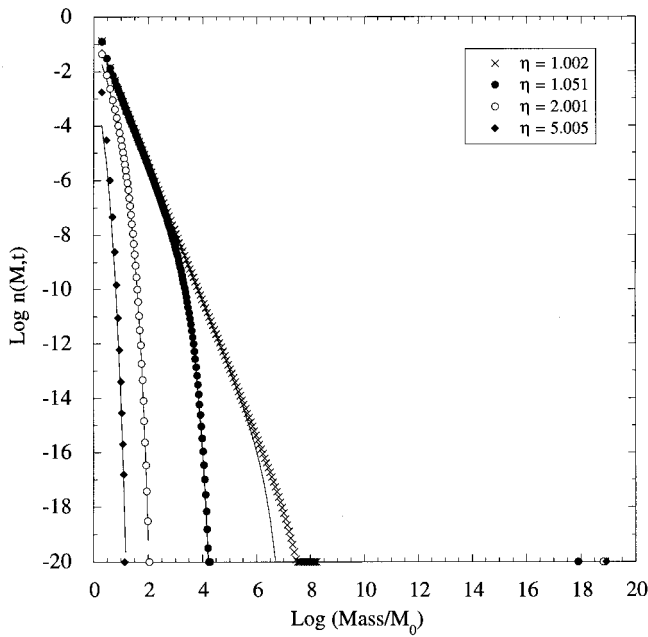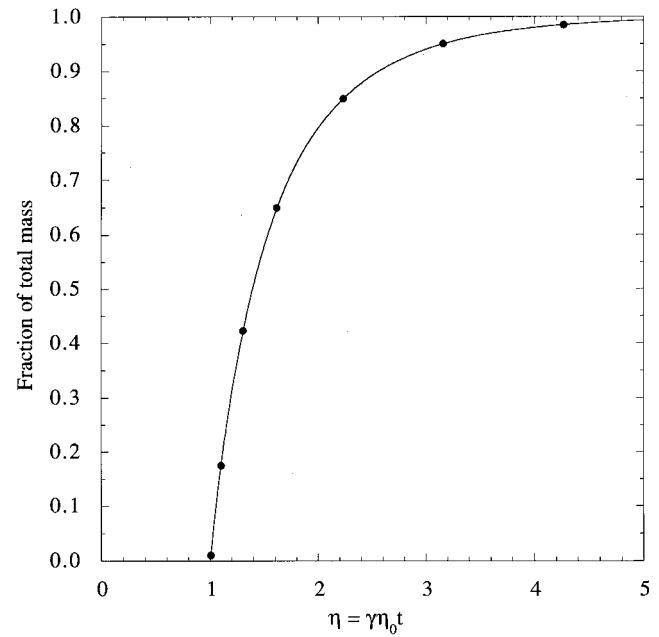
FIG. 18a

FIG. 18b

FIG. 18.—Runaway growth for $A_{ij} = \gamma_c M_i M_j$. (a) Evolution of the residual mass distribution for four values of $\eta > 1$. The simulations lag the analytic model for $\eta \approx 1$ and then follow it closely for larger η. (b) Evolution of the mass of the runaway body for the simulation (circles) and the analytic model (solid curve) as a function of η.

models have larger n_k at high masses, which reduces the time step considerably compared with models with small δ. The calculation then requires a significant amount of computer time and does not agree as well with the analytic predictions. Our models with $\delta \geq 1.4$ fail to reach $\eta_3 \approx 1.1$ if we maintain our criterion of small δn_k per time step. Relaxing this criterion allows reasonable time steps but produces very poor agreement, $\gtrsim 20\%$, with the analytic solution.

These results confirm our limits on δn_k for the Kuiper Belt simulation described in the main text, $\lesssim 0.1\%$ per time step, for $\delta = 1.08–1.4$. Models with larger δ fail to follow growth properly unless the time steps are unreasonably small.

REFERENCES

Aarseth, S. J., Lin, D. N. C., & Palmer, P. L. 1993, ApJ, 403, 351
Adachi, I., Hayashi, C., & Nakazawa, K. 1976, Prog. Theor. Phys., 56, 1756
Backman, D. E., & Paresce, F. 1993, in Protostars and Planets III, ed. E. H. Levy & J. I. Lunine (Tucson: Univ. Arizona Press), 1253
Bailey, M. 1994, in IAU Symp. 160, Asteroids, Comets, Meteors 1993, ed. A. Milani, M. Di Martino, & A. Cellino (Dordrecht: Kluwer), 443
Barge, P., & Pellat, R. 1990, Icarus, 85, 481
———. 1991, Icarus, 93, 270
———. 1993, Icarus, 104, 79
Beckwith, S. V. W., & Sargent, A. I. 1996, Nature, 383, 139
Boss, A. P. 1993, ApJ, 417, 351
Cameron, A. G. W. 1995, Meteoritics, 30, 133
Davis, D. R., & Farinella, P. 1997, Icarus, 125, 50
Duncan, M. J., Levison, H. F., & Budd, S. M. 1995, AJ, 110, 3073
Edgeworth, K. E. 1949, MNRAS, 109, 600
Fernández, J. A. 1997, Icarus, 129, 106
Fernández, J. A., & Ip, W.-H. 1981, Icarus, 47, 470
———. 1984, Icarus, 58, 109
———. 1996, Ap&SS, 44, 431
Goldreich, P., & Ward, W. R. 1973, ApJ, 183, 1051
Greenberg, R., Bottke, W., Carusi, A., & Valsecchi, G. B. 1991, Icarus, 94, 98
Greenberg, R., Wacker, J. F., Hartmann, W. K., & Chapman, C. R. 1978, Icarus, 35, 1
Greenberg, R., Weidenschilling, S. J., Chapman, C. R., & Davis, D. R. 1984, Icarus, 59, 87
Greenzweig, Y., & Lissauer, J. J. 1990, Icarus, 87, 40
———. 1992, Icarus, 100, 440
Hayashi, C. 1981, Prog. Theor. Phys. Suppl., 70, 35
Hayashi, C., Nakazawa, K., & Nakagawa, Y. 1985, in Protostars and Planets II, ed. D. C. Black & M. S. Matthews (Tucson: Univ. Arizona Press), 1100
Holman, M. J., & Wisdom, J. 1993, AJ, 105, 1987
Hornung, P., Pellat, R., & Barge, P. 1985, Icarus, 64, 295
Housen, K. R., Schmidt, R. M., & Holsapple, K. A. 1991, Icarus, 94, 180
Ida, S. 1990, Icarus, 88, 129
Ida, S., & Makino, J. 1992a, Icarus, 96, 107
———. 1992b, Icarus, 98, 28
Ip, W.-H. 1989, Icarus, 80, 167

Ipatov, S. I. 1989, Astron. Vestn., 23, 197 (English transl. Sol. Syst. Res., 23, 119)
———. 1991, AZh Pisma, 17, 268 (English transl. Soviet Astron. Lett., 17, 113)
Jewitt, D. C., & Luu, J. X. 1995, AJ, 109, 1867
Jewitt, D., Luu, J., & Chen, J. 1996, AJ, 112, 1225
Kenyon, S. J., & Hartmann, L. W. 1995, ApJS, 101, 177
Kokubo, E., & Ida, S. 1996, Icarus, 123, 180
Kolvoord, R. A., & Greenberg, R. 1992, Icarus, 98, 2
Kuiper, G. P. 1951, in Astrophysics: A Topical Symposium, ed. J. A. Hynek (New York: McGraw-Hill), 357
Levison, H. F., & Duncan, M. J. 1993, ApJ, 406, L35
Lissauer, J. J., Pollack, J. B., Wetherill, G. W., & Stevenson, D. J. 1995, in Neptune and Triton, ed. D. P. Cruikshank, M. S. Matthews, & A. M. Schumann (Tucson: Univ. Arizona Press), 37
Lissauer, J. J., & Stewart, G. R. 1993, in Protostars and Planets III, ed. E. H. Levy & J. I. Lunine (Tucson: Univ. Arizona Press), 1061
Luu, J., Marsden, B. G., Jewitt, D., Trujillo, C. A., Hergenrother, C. W., Chen, J., & Offutt, W. B. 1997, Nature, 387, 573
Malhotra, R. 1993, Nature, 365, 819
———. 1995, AJ, 110, 420
———. 1996, AJ, 111, 504
Morbidelli, A., Thomas, F., & Moons, M. 1995, Icarus, 118, 322
Nakagawa, Y., Hayashi, C., & Nakazawa, K. 1983, Icarus, 54, 361
Ohtsuki, K. 1992, Icarus, 98, 20
Ohtsuki, K., & Nakagawa, Y. 1988, Prog. Theor. Phys. Suppl., 96, 239
Ohtsuki, K., Nakagawa, Y., & Nakazawa, K. 1990, Icarus, 83, 205
Pollack, J. B., Hubickyj, O., Bodenheimer, P., Lissauer, J. J., Podolak, M., & Greenzweig, Y. 1996, Icarus, 124, 62
Ruden, S. P., & Lin, D. N. C. 1986, ApJ, 308, 883
Ruden, S. P., & Pollack, J. B. 1991, ApJ, 375, 740
Russell, S. S., Srinivasan, G., Huss, G. R., Wasserburg, G. J., & Macpherson, G. J. 1996, Science, 273, 757
Safronov, V. S. 1969, Evoliutsiia Doplanetnogo Oblaka i Obrazovanie Zemli i Planet (Moscow: Nauka) (English transl. Evolution of the Protoplanetary Cloud and Formation of the Earth and the Planets [NASA Tech. Transl. F-677] [Jerusalem: Israel Program Sci. Transl.] [1972])
Sargent, A. I., & Beckwith, S. V. W. 1993, Phys. Today, 46, 22
Silk, J., & Takahashi, T. 1979, ApJ, 229, 242

Spaute, D., Weidenschilling, S. J., Davis, D. R., & Marzari, F. 1991, Icarus, 92, 147
Stern, S. A. 1995, AJ, 110, 856
———. 1996, AJ, 112, 1203
Stern, S. A., & Colwell, J. E. 1997a, AJ, 114, 841
———. 1997b, ApJ, 490, 879
Stewart, G. R., & Wetherill, G. W. 1988, Icarus, 75, 542
Strom, S. E., Edwards, S., & Skrutskie, M. F. 1993, in Protostars and Planets III, ed. E. H. Levy & J. I. Lunine (Tucson: Univ. Arizona Press), 837
Tanaka, H., & Nakazawa, K. 1993, J. Geomag. Geoelectr., 45, 361
———. 1994, Icarus, 107, 404

Trubnikov, B. A. 1971, Dokl. Akad. Nauk SSSR, 196, 1316
von Smoluchowski, M. 1916, Z. Phys., 17, 557
Weidenschilling, S. J. 1977, Ap&SS, 51, 153
———. 1980, Icarus, 44, 172
Weidenschilling, S. J., & Cuzzi, J. N. 1993, in Protostars and Planets III, ed. E. H. Levy & J. I. Lunine (Tucson: Univ. Arizona Press), 1031
Weidenschilling, S. J., & Davis, D. R. 1992, in Lunar and Planetary Science XXIII (Houston: Lunar Planet. Inst.), 1507
Wetherill, G. W. 1990, Icarus, 88, 336
Wetherill, G. W., & Stewart, G. R. 1989, Icarus, 77, 300
———. 1993, Icarus, 106, 190 (WS93)